Wind and wave-influenced mixing and dynamics in the near-field Fraser River plume

Sam Kastner

A thesis submitted in partial fulfillment of the requirements for the degree of

Master of Science in Civil Engineering

University of Washington

2017

Reading Committee:

Alexander Horner-Devine, Chair

Jim Thomson, Chair

Nirnimesh Kumar

Program Authorized to Offer Degree:
Civil & Environmental Engineering

University of Washington

Abstract

Wind and wave-influenced mixing and dynamics
in the near-field Fraser River plume

Sam Kastner

Co-Chairs of the Supervisory Committee:
Professor Alexander Horner-Devine
Civil & Environmental Engineering

Associate Professor Jim Thomson
Civil & Environmental Engineering

Rivers play a large role in the transport of matter between ecosystems by connecting interior regions with lakes and oceans. River outflows, or plumes, constitute a significant delivery mechanism of pollutants, sediment, and nutrients to the coastal environment. Such plumes are common along the worlds coastlines, but are poorly understood and difficult to sample due to their complexity. The effects of external forcing (such as winds and waves) on river plumes is particularly understudied, but has been shown to play a role in the behavior of the plume. The Fraser River (the site of proposed and existing oil infrastructure) is a key system to understand, as its mouth is near both a major population center (Vancouver, BC) and unique coastal ecosystems.

This study presents observations of plume mixing and stream-normal momentum balances in the Fraser river plume using Lagrangian surface drifters. The Strait of Georgia commonly experiences calm to moderate winds from the Southeast and strong storm winds from the Northwest in the winter, and there are differences in plume behavior between these conditions. Under SE winds, the plume thins, spreads, and turns to the right (North) upon exiting the river mouth, mixing intensely for a short period of time. This process is dominated by a balance between stream-normal pressure gradient, Coriolis, and rotational acceleration, as previous studies have shown. Under NW winds, the plume stays thicker, narrower, and flows

directly across the Strait while forming a lateral front on its northern side, mixing at a slower rate for longer. Different momentum terms dominate under this wind condition: the stream-normal balance pits Coriolis and rotational acceleration pressure gradient against interfacial shear stress, wind stress, wave radiation stress gradient, and ambient current body force. The two configurations of the plume show that variable winds can have a substantial impact on the shape of the plume, which can lead to changes in the sea surface anomaly associated with the dome of freshwater exiting the river mouth. Additionally, while spreading causes the plume to mix intensely under SE winds, the net mixing under NW winds is larger due to the longer extent of the plume. This indicates that large spreading is not always necessary for substantial plume mixing. Understanding the conditions that change plume mixing and behavior is a critical step in describing the pathways of pollutants, sediment, and nutrients as they enter the coastal ecosystem through a river plume.

TABLE OF CONTENTS

LIST OF FIGURES

LIST OF TABLES

ACKNOWLEDGMENTS

I cannot hope to thank all of the friends, family, and colleagues who have supported me through the process of producing this thesis. They have bolstered my confidence at every turn.

During my time at the University of Washington, I have been the beneficiary of a remarkable work environment in the Environmental Fluid Mechanics research group. Conversations with my fellow lab members helped enormously in the preparation of this thesis. I owe a special debt of gratitude to my fellow students for their support.

Alex Horner-Devine and Jim Thomson presented me with an incredible opportunity when they took me on as a student. Their encouragement, patience, and guidance made this work possible. I could not ask for better mentors. I would also like to thank Nirnimesh Kumar for his contribution of ideas, guidance, and humor.

I am grateful for the support of my family, both Rochester and Seattle contingents, throughout the process of completing this thesis. My mother, father, and sister have been extraordinarily encouraging (and available for phone calls at all hours of the day).

I would additionally like to thank NSF Grant OCE-1459051 for providing funding for this project. Rich Pawlowicz and Mark Halvorsen (UBC) provided helpful local knowledge. The observational program would not have been possible without the technical expertise of Joe Talbert, Alex DeKlerk, and Captain Andy Reay-Ellers of the University of Washington Applied Physics Lab.

Chapter 1

BACKGROUND & METHODS

1.1 Introduction

Rivers are the great connectors of the natural environment, flowing from their sources in the mountains through valleys or plains to their terminus in the ocean. As water travels from snowpack to sea, it encounters a variety of ecosystems and built environments. Flowing through these environments can result in high concentrations of sediment, nutrients, and pollutants in the river. These concentrations can vary with the season and events, such as storms, floods, and spills. For example, the Eel River, in northern California, experiences strong floods leading to discharge up to 12,000 m^3/s (summer minimum discharge can be as low as 4 m^3/s, USGS). These floods are associated with high sediment concentrations in the river water and on the shelf [Geyer et al., 2000]. In the central and eastern United States, the Mississippi River drains 40% of the lower 48 states, an area of over 3,000,000 km^2 (National Parks Service). This area includes the Great Plains, home of much of the country's agricultural production. During the spring freshet, high discharge in the Mississippi system can carry agricultural nutrients from the interior of the North American continent to the Gulf of Mexico, where it routinely forms a dead zone occupying much of the Texas-Louisiana shelf [Zhang et al., 2012]. In southwestern Canada, the proposed Trans Mountain pipeline from Edmonton to Vancouver would come within 100 m of the Fraser River in its lower reaches, and cross tributaries to the river many times upstream [Hoekstra, 2013]. This creates the potential for an oil spill into the river water, which could negatively affect salmon runs, as well as the marine environment in the river and the Strait of Georgia.

It is thus important to understand the processes that drive mixing of plume water into ambient coastal water. In the United States, 39% of the population lives in a county on the

coast (NOAA). Many of the large population centers in these coastal areas are located at or near river mouths, such as New York City, Boston, Seattle, and New Orleans. Thus materials transported from upstream can have an effect on the coastal ecosystem and economy as they mix into shelf water. Suspended sediment, as is present in the Eel River plume, can change the amount of light available to phytoplankton for photosynthesis, which impacts the local food web. The large dead zones on the Texas-Louisiana shelf due to agricultural runoff from the Mississippi plume have a negative impact on local fisheries and economies. NOAA has estimated that dead zones cost the U.S. seafood and tourism industry $82 million each year. Oil and pollutant spills or releases can cause extreme damage to fragile coastal marine ecosystems. Such contamination has been common in the United States, as an EPA report released in 2013 found that 55% of streams and rivers in the US are in poor condition for aquatic life. Global- and basin-scale numerical models currently do not resolve plume effects well, and so a clear understanding of these effects is necessary to parameterize this subgrid scale process [Sharples et al., 2017]. Smaller scale numerical models more accurately predict plume behavior, but a better understanding of mixing and dynamics in plume systems is necessary to improve forecasting of and response to pollutant spills, nutrient outflow, and sediment loads in coastal and riverine ecosystems.

Much attention in the scientific community has been devoted to understanding plume mixing driven by spreading and shear in the near- and mid-field of the plume structure [MacDonald and Geyer, 2004, McCabe et al., 2008, Hetland, 2010], and wind-driven mixing due to Ekman processes in the far-field [Fong and Geyer, 2001, Lentz, 2004]. An underlying assumption of most near-field dynamics studies has been that the wind is relatively unimportant [McCabe et al., 2009, Chen et al., 2009, Kilcher et al., 2012]. Some studies have examined the impact of wind and wave forcing on the dynamics and spreading of plumes in the far-field, and others have studied wave-driven turbulence in the open ocean, but questions about the effects of wind and wave forcing on near-field plume dynamics and mixing remain unanswered.

Mixing in the near-field plume is thought to be the strongest in the plume system, with

associated turbulent kinetic energy dissipation rate values as high as 10^{-3} m^2/s^3 [MacDonald and Geyer, 2004, MacDonald et al., 2007, Kilcher et al., 2012]. This mixing and turbulence is caused by increased velocity shear as the fresh river water lifts off the bottom, compressing the river flow into a shallower layer. This increased shear causes the local Richardson number to decrease, and mixing and turbulence to intensify to a near-field peak near liftoff [MacDonald et al., 2007, McCabe et al., 2008]. Seaward of the liftoff point, entrainment of low-momentum, high-density ambient water decreases the shear present in the surface plume layer, increasing Richardson number. However, as the river exits its mouth, it is no longer laterally constrained and spreads. Spreading is predominantly controlled by a competition of stream-normal pressure gradient and Coriolis forces [McCabe et al., 2009] (MC09). In order for mass to be conserved, the plume speeds up and thins as it spreads, thereby increasing shear. So, as the plume expands, its mixing and dynamics can be described as the acceleration due to spreading competing with the deceleration due to mixing [Hetland, 2010, Horner-Devine et al., 2015]. As the aspect ratio of a river plume is typically small ($h_p/L = \mathcal{O}(10^{-3})$, where h_p is the depth of the plume and L is the horizontal length scale of the plume), most mixing occurs via the vertical turbulent flux of density through the base of the plume [Horner-Devine et al., 2015]. As the plume spreads, this base area increases, increasing the area over which mixing can occur [Yuan and Horner-Devine, 2013]. Observations of the near-field Merrimack River plume show that spreading can also be described by the stretching of a Kelvin-Helmholtz instability along its rotational axis, leading to a relationship between plume spreading and the energy contained in such an instability [MacDonald and Chen, 2012]. This theory has also been shown to be valid in the Connecticut River estuary [Geyer et al., 2017].

Wind has generally been assumed to have a minimal direct effect on mixing in energetic plume regions such as the near-field, and is often neglected in near-field studies (some exceptions are noted in the following paragraph). In the far-field, wind-driven plume mixing has been characterized as an Ekman-driven process. Numerical models show upwelling wind can mix a plume of uniform depth to a critical depth set by Ekman transport, mass

conservation, and the critical bulk Richardson number while spreading the plume offshore, confirming an analytical model [Fong and Geyer, 2001]. Once the far-field plume reaches this critical depth, mixing is suppressed. Modifications to this model show similar behavior in the presence of more complex geometry and larger scales (using analytical and numerical techniques, respectively) [Lentz, 2004, Hetland, 2005]. These modifications compare well to the results of Fong and Geyer results and observations from the Chesapeake Bay buoyant coastal current.

Wind and ambient currents have also been shown to advect a plume on various geometrical scales. An observational study shows that the far-field Columbia River plume responds quickly to wind forcing, behaving as a geostrophic current under wind forcing [Hickey et al., 1998]. Closer to the mouth the plume may be advected north or south by corresponding winds [Hickey et al., 1998]. Wind and ambient flow forcing can also change the plume's stable seasonal orientations, enhance the stability of a seasonal orientation, or split the plume into two outflows [García Berdeal et al., 2002, Hickey et al., 2005]. Additionally, an analytical framework for the influence of winds on plume geometry in the far-field compares well to observations of the Chesapeake Bay buoyant coastal current [Lentz and Largier, 2006]. This framework shows that downwelling winds pin the plume to the coast, leading to a vertically mixed (but still relatively fresh) water mass, with inhibited mixing relative to upwelling winds (depending on wind strength). In different dynamic regions of a large scale river plume, wind can have different effects, and can even stop the accumulation of water into the plume bulge region [Horner-Devine et al., 2009]. Closer to the river mouth, Hunter et al. [2010] and Kakoulaki et al. [2014] have studied the effects of the wind on the near-field plume. Advection and mixing in the Hudson River plume can be changed by the diurnal sea breeze, particularly under neap tide and strong discharge conditions when the plume is shallow and highly stratified [Hunter et al., 2010]. The sea breeze traps the Hudson plume by the Long Island coast, where it forms a recirculating bulge. The Merrimack River plume is strongly affected in its near- and mid-field by moderate wind forcing (>4 m/s) [Kakoulaki et al., 2014]. Despite the wind influence shown in these studies, near-field plume momentum

balances typically ignore wind input.

The dominant terms of the plume momentum balance vary across the spatial scales of a river plume [Horner-Devine et al., 2015]. In the near-field, a numerical model of the Columbia River plume shows that the streamwise momentum balance is controlled by forces associated with advection, pressure gradient, and interfacial shear stress, while the stream-normal momentum balance is controlled by centrifugal, stream-normal pressure gradient, and Coriolis forces. For both momentum balances, winds did not contribute significantly [McCabe et al., 2009]. A numerical model of the Merrimack river plume shows similar results for the stream-normal momentum balance and reveals that interfacial shear stress affects the plume spreading close to the river mouth [Chen et al., 2009]. Cross-shore momentum balances from observations in the near-field of the Columbia plume using a control volume technique show that during high flow (Q = 12000 m^3/s) and strong ebb, the interfacial shear stress divergence is the dominant source of plume deceleration [Kilcher et al., 2012]. As the ebb lessens, pressure gradient and Coriolis forces become important. For weaker flow ($Q = 4000$ m^3/s), stress is still an important factor in decelerating the plume.

Breaking waves are a significant source of near-surface oceanic turbulence [Craig and Banner, 1994, Melville, 1996, Terray et al., 1996]. Turbulence due to wave breaking is typically associated with dissipation values of $\mathcal{O}(10^-3)$ at the near-surface [Terray et al., 1996, Gemmrich, 2010, Thomson, 2012, Zippel and Thomson, 2015, Thomson et al., 2014]. This turbulence is found to decay in magnitude exponentially beneath the surface [Terray et al., 1996, Gemmrich, 2010, Feddersen, 2012a,b, Thomson et al., 2013, 2016, Zippel and Thomson, 2015]. This turbulence, ϵ_{wave}, scales with the wave height H_{sig}, normalized depth $(z/H_{sig})^{-\lambda}$ (where $\lambda = -2$), and an input parameter G [Terray et al., 1996]. This parameter, which functions as the surface boundary condition for the turbulence, has been found to scale with the wind friction velocity u_*^3 under wind forcing [Gemmrich, 2010]. A scaling for G based on wave energy flux gradient dF/dx, H_{sig}, depth d, and an exponential function of normalized depth compares well with observations [Feddersen, 2012b, Zippel and Thomson, 2015]. Wave steepness is conventionally defined as $(H_{sig}k_p)/2$, and is a controlling parameter in wave

breaking processes [Banner et al., 2000]. This increase in steepness due to wave-current interaction leads to observed increased wave breaking at the Columbia River plume front, and the resulting turbulence could conceivably mix the plume [Thomson et al., 2014]. In the presence of following or opposing currents, waves are lengthened or shortened, respectively. In wave-current interaction, the absolute wave frequency ω is conserved such that

$$\omega = \sigma + \vec{u} \cdot \vec{k}, \tag{1.1}$$

where $\vec{u}$ is the current, k is the wavenumber, and $sigma$ is the intrinsic frequency from the linear dispersion relation $\sigma^2 = gktanh(kd)$, with d being the depth. It can be shown analytically that waves are blocked by an opposing current when the group velocity of the waves, $c_g = \frac{\partial \omega}{\partial k}$, is greater than or equal to half of the current u [Mei, 1989]. However, waves typically break due to a limiting steepness for $u < c_g/2$ [Chawla and Kirby, 2002].

Wave breaking in the far-field plume leads to a thicker, narrower, more vertically homogeneous plume than would be expected under upwelling wind conditions [Gerbi et al., 2013]. Generalized plume model simulations with wave breaking also show more intense mixing than those without; these simulations also show that the analytical framework from Lentz [2004] under predicts the rate of plume thickening in simulations with wave-breaking [Gerbi et al., 2013]. Model simulations of the Mississippi-Atchafalaya plume agree with these results [Rong et al., 2014]. Gerbi et al. [2015] examine the thickening rate under wind and wave forcing using a one-dimensional numerical model, and show that wave breaking can hasten the thickening of the surface boundary layer (such as a far-field plume), especially when rotational effects are considered. Observations of the Columbia River plume front show that the plume front is capable of blocking an opposing wind sea and that turbulence is elevated when this occurs [Thomson et al., 2014]. Wave-breaking turbulence that is downwelled at the plume front could elevate the levels of turbulence at the plume base, leading to increased mixing. Numerical modeling of the Columbia River plume shows that waves can translate the plume hundreds of meters in the down-wave direction due to Stokes drift-driven horizontal salt advection [Akan et al., 2017].

In the following sections, I detail the methods of the observational program, describe the observed meteorological conditions and their associated plume behavior, and perform mixing and momentum balance calculations. I use the results from these calculations to make inferences about the role of waves in mixing the plume, the total amount of mixing under varying winds, the validity of current plume mixing theories, and the effects of spreading (or lack thereof) on the pressure gradient in the plume.

1.2 Observational Program and Methods

1.2.1 Geographical Setting and Conditions

The Fraser River drains an area of greater than 230,000 km^3 in western British Columbia, Canada, and is one of the longest river systems in the country at 1,370 km. Its highest flows of around 10,000 m^3/s (measured at Hope, BC) occur during the June freshet, and low flows ranging from 500 to 1000 m^3/s occur between February and April. The river flows into the Strait of Georgia approximately 20 km south of Vancouver, over a network of tidal flats that are exposed at low water (Fig. 1.1a). A jetty extends to the western edge of these tidal flats at Sand Heads (10 km offshore at high water) on the northern side of the river channel, which is maintained by dredging to a depth of 10 m (Fig. 1.1a). The channel bends SW at a right angle at the 4 km marker in the channel, forcing the outflow to exit the channel perpendicular to the southeasterly ebb tidal velocity of the Strait.

Tides in the Strait of Georgia are dominated by a mixture of semi-diurnal and diurnal constituents. During the sampling period, tidal amplitudes ranged from approximately 1-4m (Fig. 1.1d). Tidal currents recorded at Puffin Island Light (south of the Fraser River mouth) were as high as 0.5 m/s on both flood and ebb. At the river mouth, observed surface currents varied from 1.5 to 2.5 m/s at maximum ebb tide. During the lower flow conditions of winter, the fresher surface flow at Sand Heads has a characteristic salinity between 4 and 15 psu depending on discharge. The river flow to lifted off the riverbed 20 km upstream of Sand Heads, forming a salt wedge with salinity 25 psu.

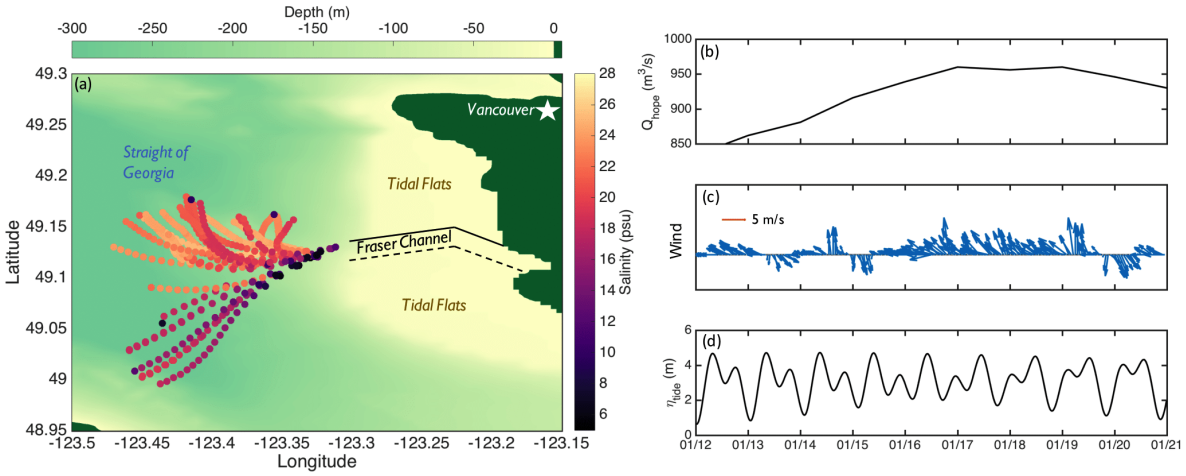

Figure 1.1: (a) shows SWIFT drift tracks between January 16 and 20, when SWIFTs were released from the river mouth. Points are colored by 0.5 m salinity measurements and background color shows depth; (b)-(d) are time series during the study period of (a) discharge from the Fraser River at Hope gauging station (Environment Canada); (b) median Sand Heads wind speeds and directions for each day and (c) tidal stage, Sand Heads station (Environment Canada).

In the winter, wind conditions in the Strait of Georgia are close to bimodal, with weak to moderate winds (5-7 m/s) out of the southeast the predominant condition; however, winter storms in the region typically cause stronger northwest wind velocities (10 m/s, Fig. 1.1a). The fetch to the river mouth at Sand Heads under NW wind conditions is longer on average than under SE wind conditions due to the quasi-elliptical geometry of the Strait. This longer fetch results in larger waves under NW wind conditions.

During the study period, the Fraser streamflow gauge at Hope, BC, measured discharges varying between 850 and 960 m^3/s, with larger discharges toward the end of the study (Fig. 1.1a). This coincides with larger daylight ebbs, as the tidal phase shifted over the course of the study by approximately one-half of a neap-spring cycle (Fig. 1.1c).

Observations show wind speed variation between 3 and 10 m/s from a variety of wind directions (Fig. 1.1b). Under consistent stronger wind forcing ($>$ 5 m/s, January 16-20), this variable directionality sorts into forcing from the SE, E, and NW. The resulting wave conditions under SE and NW winds follow the fetch relationship outlined above, with larger waves under SE winds (Table 1.1).

1.2.2 Observations

A group from the University conducted fieldwork in the southern Strait of Georgia between January 12 and 21, 2016. Ship-based observations were taken from the *R/V Jack Robertson* (University of Washington Applied Physics Lab), and Surface Wave Instrument Float with Tracking (SWIFT) drifters [Thomson, 2012] to performed Lagrangian observations under ebb tidal conditions. An Acoustic Waves and Currents (AWAC) mooring was placed to the NW of the river mouth to measure wave height and surface currents upstream (relative to the tidal current in the Strait) of the plume.

Two SWIFT models were deployed: the version 3 models, which are fully instrumented, durable buoys, and the prototype version 4, which featured a stripped-down instrumentation. The version 3 SWIFTs collect salinity and temperature data using either one or three Aanderaa 4319, mounted on the drifters hull at 0.5 m or 0.2, 0.5, and 1.2m, respectively.

Table 1.1: Observed conditions

Parameter	17 January 2016	19 January 2016
Tidal amplitude (m)[a]	2.89	3.3
Hours after high water	4.25	5.3
Mean wind speed (m/s)[b]	7.2	8.4
Max wind speed (m/s)	9.2	12.3
Mean wind direction (°N)	127	284
Significant wave height (m)	0.7	1.1
Peak wave direction (°N)	104	317
River discharge (m^3/s)[c]	956	946

(a) Tidal conditions from Sand Heads (Environment Canada), hours after high water indicates time of deployments.

(b) Wind and wave conditions from SWIFTs.

(c) Discharge from Fraser at Hope gauging station (Environment Canada).

The version 3 measures wave spectra and bulk properties using either its GPS or IMU unit; the GPS is also used to calculate position, drift speed, and drift direction. The SWIFTs hull-mounted Nortek Aquadopp [1 MHz] ADCP can be used to measure either velocity shear (downlooking configuration, two drifters) or near-surface turbulent dissipation rate using a structure function method.

The prototype version 4 SWIFT uses a downlooking Nortek Signature [1 MHz] ADCP to measure velocity shear and turbulent dissipation rate [Paris and Thomson, 2017]. The version 4 SWIFT was also equipped with two GPS units used to measure position, drift speed, and drift direction. During the deployments explored in this paper, a line with up to six YSI Sonde 600LS CTDs was attached to the version 4.

The SWIFTs were deployed in pairs each day, typically just before or at the time of maximum ebb tide velocity at Sand Heads. During the deployments shown in this work, these pairs of SWIFTs were released in three different cross-channel positions (200 m apart) to capture the spatial range of the plume. These deployments typically lasted 4-6 hours and were accompanied by ship-based measurements taken from the Robertson.

The Robertson was equipped with two ADCPs: a pole-mounted RDI 1200 kHz ADCP and a hull-mounted RDI 300 kHz ADCP. To capture density changes, CTD casts were performed using a Seabird 19plus and recorded surface salinity using a pole-mounted Aanderaa 4319.

1.2.3 Mixing Methods

Previous work in MacDonald and Geyer [2004] and McCabe et al. [2008] (MC08) establishes a control volume formulation based on salt conservation to calculate salt flux through the base of the plume. By assuming the system can be described as a slab of fresher water flowing over an ambient saltier layer, I can calculate vertical salt flux through the base of the fresher layer if I take the layer as a control volume. Assuming the plume is steady over the course of a drift track, a pair of drifters released at the same time trace out plume streamlines, spreading as they travel with the fresher water layer. If I assume no stream-normal contributions to mixing (outlined in the appendix of MacDonald and Geyer [2004]),

then any along-track (streamwise) change in the salt budget must originate from turbulent mixing at the bottom of the control volume. This relationship can be described by

$$S_e w_e = \frac{1}{B}\frac{\partial}{\partial s}(uhBS), \tag{1.2}$$

where $S_e w_e$ is the salt flux through the bottom of the control volume (described as an entrained salinity, S_e, multiplied by the entrainment velocity, w_e, at the plume base), u is the velocity of the plume water, B is the distance between the drifters, h is the depth of the base of the slab layer, S is a representative plume salinity, and $\frac{\partial}{\partial s}$ represents the derivative in the streamwise direction [McCabe et al., 2008].

I use SWIFT drift speed as plume velocity u, SWIFT 0.5m salinity as S, and the separation between a pair of co-released SWIFTs as B. The 0.5 m CT measurement from each SWIFT is a valid representation of the plume salinity, as it is the freshest plume water that could mix with the water below. In order to find a representative h, I combine salinity measurements from the CTD chain attached to the SWIFT v4b and near-surface salinity from SWIFTs with three CTs. The combination of these measurements gives information about salinity down to 4 m. After vertical interpolation and smoothing, I pick h as the depth of the 21 psu isohaline. While the surface plume water is continuously stratified, the depth of the 21 psu isohaline appears to be a point of inflection for the vertical salinity and velocity structure (Fig. 1.2), and is consistently observed by drifter salinity measurements over the length of most deployments. Thus, $S_e = 21$. I do observe slight variability of S and u between drifters in a pair, and therefore make the mixing calculation using smoothed mean S and u values over the two drifters, while using the pairs smoothed B values and the plume-wide smoothed value of h. I calculate streamwise gradients relative to the arc length of the drifter track.

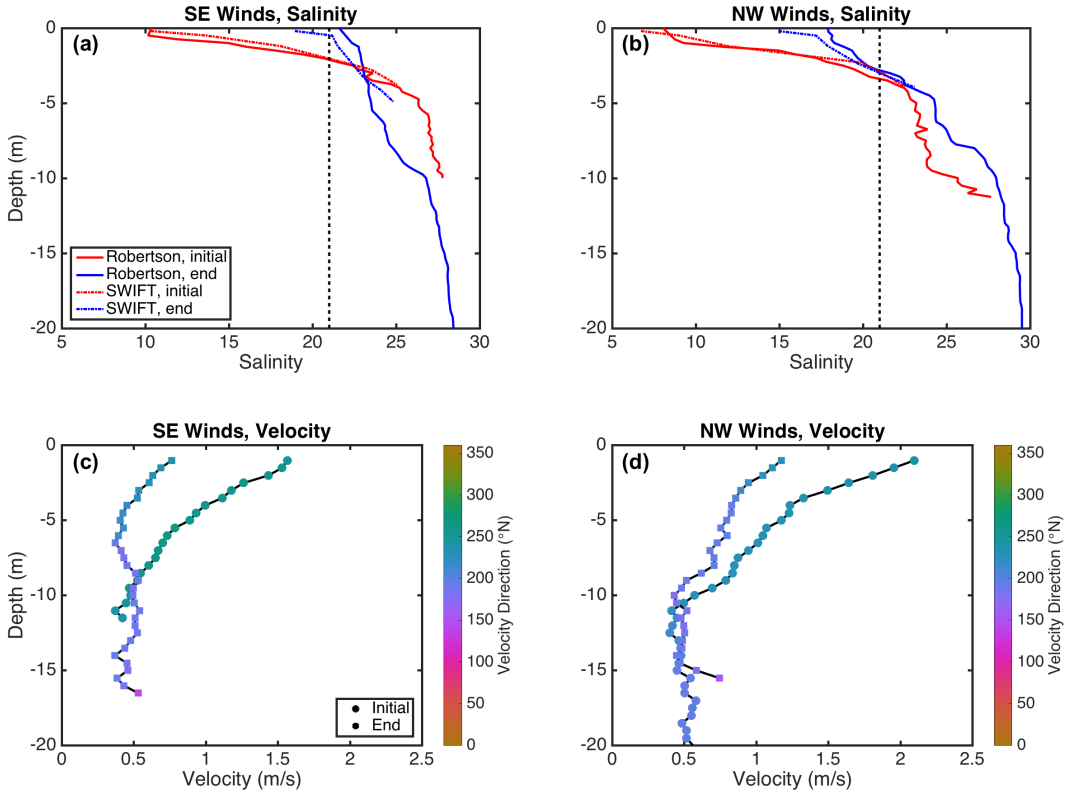

Figure 1.2: Profiles of salinity and velocity for beginning and end of drift tracks for each condition. Panels (a) and (b) show salinity profiles for SE and NW winds, respectively. Red lines indicate initial conditions and blue lines indicate conditions at the end of the drift near the drifter recover location. Solid lines indicate casts from the *Robertson* CTD and dash-dotted lines indicate profiles from the SWIFT v4β's CTD chain. Panels (c) and (d) show velocity profiles for SE and NW winds, respectively, from the shipboard ADCP. Circle markers indicate initial profiles and square markers indicate profiles from the end of a drift near the drifter recovery location. Color indicates velocity direction in degrees from north.

1.2.4 Momentum Balance Methods

In order to effectively capture the plume dynamics, I calculate momentum balances in a streamwise versus stream-normal reference frame [Hench and Leuttich, 2003]. However, the dynamics I expect from the Fraser system are different from the inlet dynamics described in Hench and Leuttich [2003] due to the presence of stratification and lack of bottom attachment of the plume [McCabe et al., 2009]. These calculations differ from those of MC09 in that SWIFT measurements are in the Lagrangian reference frame, so I derive a new set of s-n momentum equations using the appendix of Hench and Leuttich [2003]. I neglect horizontal viscous terms, as these are not able to be resolved with localized Lagrangian drifter measurements, and the small aspect ratio of the plume ($\frac{h}{L} \approx 10^{-3}$). I integrate these equations vertically over the depth of the 21 psu isohaline to find the momentum balance in the buoyant layer,

$$0 = \overbrace{h_i \frac{DU_s}{Dt}}^{\substack{\text{streamwise} \\ \text{Lagrangian} \\ \text{acceleration}}} + \overbrace{\frac{h_i}{\rho_{ref}} \frac{\partial P}{\partial s}}^{\substack{\text{streamwise} \\ \text{pressure} \\ \text{gradient}}} - \overbrace{\frac{\tau_0^s - \tau_i^s}{\rho_{ref}}}^{\substack{\text{streamwise} \\ \text{stress} \\ \text{divergence}}} + \overbrace{\frac{(\tau_0^n - \tau_i^n)(\alpha_0 - \alpha_i)}{\rho_{ref}}}^{\substack{\text{normal stress} \\ \text{contribution through} \\ \text{vertical veering}}} \tag{1.3}$$

$$0 = \underbrace{h_i U_s \frac{D\alpha}{Dt}}_{\substack{\text{rotary} \\ \text{Lagrangian} \\ \text{acceleration}}} + \underbrace{h_i f U_s}_{\substack{\text{Coriolis} \\ \text{acceleration}}} + \underbrace{\frac{h_i}{\rho_{ref}} \frac{\partial P}{\partial n}}_{\substack{\text{stream-normal} \\ \text{pressure} \\ \text{gradient}}} - \underbrace{\frac{\tau_0^n - \tau_i^n}{\rho_{ref}}}_{\substack{\text{stream-normal} \\ \text{stress} \\ \text{divergence}}} - \underbrace{\frac{(\tau_0^s - \tau_i^s)(\alpha_0 - \alpha_i)}{\rho_{ref}}}_{\substack{\text{streamwise stress} \\ \text{contribution through} \\ \text{vertical veering}}} \tag{1.4}$$

where subscripts i and 0 denote values at the 21 psu isohaline ("interface" from here) and the near-surface values, respectively. Subscript s denotes a streamwise value, $\frac{\partial}{\partial s}$ and $\frac{\partial}{\partial n}$ denote streamwise and stream-normal partial derivatives, respectively, and $\frac{D}{Dt}$ indicates the total Lagrangian time derivative in the SWIFT reference frame. Thus, h_i indicates the depth of the 21 psu isohaline, U_s is the streamwise velocity, ρ_{ref} is a reference density taken as 1021 kg/m^3 ($S = 26psu, T = 5°\text{C}$), P is pressure, τ is a stress applied in the streamwise

or stream-normal direction at either the surface or the interface, and α is the direction of the streamline at either the near-surface or interface. Since I make these calculations over a surface plume layer assumed to have a uniform value of velocity, I take α to be constant with depth such that $\alpha_0 = \alpha_i = \alpha_{mean}$.

I calculate stream-normal momentum balances from pairs of SWIFTs released together. Below I describe the decomposition of the momentum equation into forcing terms for the acceleration, Coriolis, wind stress, and interfacial shear stress. In this method, pressure gradient is a residual term. Acceleration, Coriolis, and wind stress as the means of these terms for a SWIFT pair, while interfacial shear stress is calculated for SWIFTs with a downlooking ADCP. Wave radiation stress gradient and ambient current form drag are calculated using a mixture of data sources, as described below.

To calculate rotary Lagrangian acceleration, I take $h_i U_s$ as the vertical integral from the surface to the depth of the 21 psu isohaline, using downlooking ADCP currents from SWIFTs v4β and 09 (for SE and NW conditions, respectively) combined with SWIFT drift speed to create a profile of velocity to integrate. The value $\frac{D\alpha}{Dt}$ is calculated as the time derivative of SWIFT drift direction.

I calculate the Coriolis acceleration by taking the value of $h_i U_s$ already found and multiplying it by the Coriolis parameter $f \approx 1.1 \times 10^{-4}$ for 49.1° N latitude.

To find the surface stress term, I first assume that the wind stress is the only stress applied to the surface of the plume. Distributing the stream-normal stress divergence and veering stress (contribution of the streamwise stress to the stream-normal momentum through streamline curvature variation) terms, the wind stress term can expressed as

$$M_{wind} = -\frac{\tau_0^n}{\rho_{ref}} \tag{1.5}$$

taking the surface stress $\tau_0 = \rho_a C_d U_{10}^2$, where $\rho_a = 1.225$ kg/m^3 is the density of air, $C_d = 1.5 \times 10^{-3}$ is a typical sea-surface drag coefficient, and U_{10} is the velocity at 10 meters. U_{10} is calculated based on 1 m SWIFT wind measurements by extrapolating SWIFT measurements using an assumed wind speed log-layer.

I use similar logic to find the interfacial shear stress term, assuming there are no other interfacial stresses,

$$M_{shear} = \frac{\tau_i^n}{\rho_{ref}} \tag{1.6}$$

taking the interfacial stress $\tau_i = \rho_0 C_{di} \Delta u^2$, where ρ_0 is the density of the surface plume layer (taken from each SWIFT's CT measurement), Δu^2 is the difference between the velocity in the surface plume layer and the velocity just below the 21 psu isohaline, calculated from downlooking SWIFT current profiles, and C_{di} is the interfacial drag coefficient. I take the interfacial drag coefficient to be

$$C_{di} = Ri_b^{3/2} \frac{(Ri_b^{-1} - Ri_c^{-1})(Ri_b^{-1/2} - Ri_c^{-1/2})}{96}, \tag{1.7}$$

where I take the critical bulk Richardson number to be $Ri_c = 1$ [Jurisa et al., 2016]. This parameterization is based on the kinetic energy available to create a turbulent overturn and the timescale related to the growth rate of Kelvin-Helmholtz instabilities Jurisa et al. [2016]. This critical bulk Richardson number threshold dictates that I do not calculate a drag coefficient for subcritical bulk Richardson number, and thus do not calculate a stress.

I assume that the residual from this balance is equal to the unresolved forcing on the plume with a major contribution from the pressure gradient. It also includes the error associated with each term. The pressure gradient signal included in the residual takes into account all pressure input into the momentum balance, including barotropic pressure gradient, baroclinic pressure gradient, and a form drag from the ambient current in the Strait. The residual also includes other forcing, such as a wave radiation stress gradient caused by wave breaking at the plume front.

Section 3.4 details the effects of including the ambient current form drag and wave radiation stress gradient in the stream-normal momentum balance (removing them from the residual). I use the methods below to calculate these momentum contributions.

Wave forcing on the plume can be incorporated in the momentum balance as a horizontal gradient of wave radiation stress as waves break at the plume front. This radiation stress,

S_{nn}, is the momentum flux carried by the waves and can be calculated as

$$S_{nn} = \frac{1}{16}\rho g H_{sig}^2 (\frac{2k_e d}{\sinh(2k_e d)} + \frac{1}{2}), \tag{1.8}$$

where H_{sig} is the significant wave height, k_e is the energy wavenumber, and d is the water depth. In order to compute a gradient of S_{nn}, I must assume that waves are breaking and losing momentum flux across a front of width equal to two wavelengths; this is approximately what I observed visually from the deck of the *R/V Robertson*, $n_{front} \approx 50$m. To calculate S_{nn}^{out}, the radiation stress outside of the plume, I use H_{sig} and k_e data from the first 10-minute average recorded by SWIFT 11, which was deployed outside of the front. Over the course of the ∼2 hour deployment the front overtook the drifter, thus I use only the initial data. Assuming a steady wave field outside the plume during the deployment, I calculate $\frac{\partial S_{nn}}{\partial n} = (S_{nn}^{out} - S_{nn}^{in})/n_{front}$, where I find S_{nn}^{in} using H_{sig} and k_e from SWIFT 15, inside the plume (see Appendix A1).

I observed a relatively large (60 cm/s) ambient surface current in the Strait of Georgia under NW winds, likely resulting from the superposition of a wind-driven current on top of the southeastward ebb tidal velocity. In order to incorporate this effect into the momentum balance, I make a simple control volume momentum conservation calculation. On the upstream (with respect to the ambient flow) end of the control volume, the current has an average velocity u_1 over a depth H. On the downstream end, the current has an average velocity u_2 over a depth $H - h$, where h is the thickness of the surface plume layer with the plume velocity directed into the page. If no momentum was lost on impact with the plume layer, I would expect $u_2 = \sqrt{(H-h)u_1^2/H}$. Thus, a momentum input through the current form drag on the plume, M_{Ac}^n, may be calculated such that

$$M_{ac}^n = \frac{u_1^2}{H} - \frac{u_2^2}{H-h}. \tag{1.9}$$

This form drag is a part of the pressure term in the momentum balance. O'Donnell et al. [1998] predict that a baroclinic pressure gradient at the plume front due to frontal tilt will compensate for momentum input due to frontal convergence. From CTD casts on either

side of the plume front, I observe this baroclinic pressure gradient to be $\mathcal{O}(10^{-5})$, and the momentum input from the ambient current to be $\mathcal{O}(10^{-4})$. Thus I include the ambient current form drag in the stream-normal momentum balance.

Chapter 2

RESULTS & DISCUSSION

2.1 Results

2.1.1 Observed Plume Behavior

Drifter trajectories under the conditions outlined above vary greatly for drifters released at Sand Heads (Fig. 1.1d). For an individual day, drifters would tend in similar directions, but over the course of the five days shown in Fig. 1.1d, the drift tracks appear to span much of the southern Strait of Georgia. In addition to drift trajectory, average salinity over a SWIFT burst changes depending on the day and location in the plume. In order to determine the mechanism causing this variability, I examine the most disparate conditions for the remainder of this paper. These occur on 17 January 2016, with SE (downwelling) winds, and on 19 January 2016, with NW (upwelling) winds (Table 1.1, Fig. 2.1). Table 1.1 shows that discharge, tidal stage, deployment time relative to high tide, and mean wind speed between the days are consistent, while maximum wind speed, wind direction, and the resulting significant wave height and direction differ. On 17 January, the SWIFTs reported a mean maximum wind speed of 7 m/s out of the southeast, and on 19 January a wind speed of 8 m/s out of the northwest (see table 1.1). The discharge and tidal amplitude were similar on each day, and drifters were deployed just after max ebb (measured at Puffin Island Light). These winds resulted in larger wave heights under NW winds conditions and a corresponding change in wave direction.

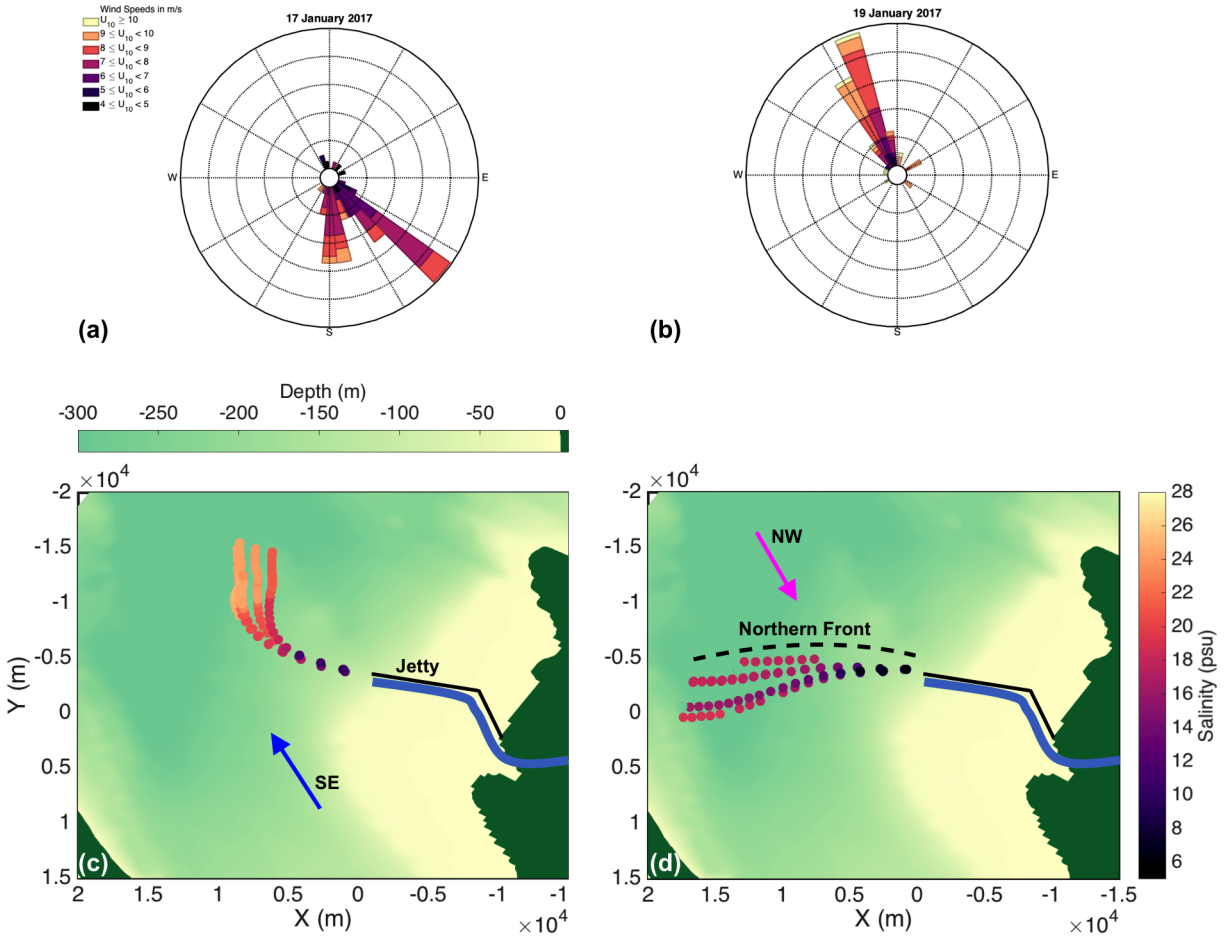

Figure 2.1: Wind roses and drifter track maps (colored by salinity) for two different days. Wind roses show relative prevalence of various wind speeds and directions. Points on maps indicate 12-minute SWIFT burst averages of position and salinity. Panel (a) shows the wind rose for 17 January 2016. Panel (b) shows the wind rose for 19 January 2016. Panel (c) shows drifter tracks from 17 January 2016, when winds were out of the southeast, as indicated by the large blue arrow. Panel (d) shows conditions from 19 January 2016, when winds were out of the northwest, as indicated by the large magenta arrow. The location of the northern front in (d) is approximate.

2.1.2 Plume Response to SE and NW Winds

These opposite wind and wave conditions coincide with contrasting plume behaviors. Drifters observed different behavior in drift speed, the 21 psu isohaline depth, spreading characteristics, and salinity over the length of a drift track under each condition (Fig. 2.2a-d). The drift speed decreased from similar values along track for each day, but did so more slowly under NW winds. Additionally, under SE winds, the drift speed at the end of the deployment was 0.5 m/s, but under NW winds was 1 m/s. The 21 psu isohaline shoaled rapidly along track under SE winds, whereas under NW winds it stayed deeper throughout the deployment. A nondimensional spreading and spreading rate parameter, $\frac{B_0}{B}\frac{\partial B}{\partial s}$ (where B_0 is the initial distance between drifters), shows that the drifters spread more relative to their initial and current distance apart during a peak under SE winds (Fig. 2.2c), while a more consistent smaller value was observed under NW winds. Salinity increased under each condition, with a higher initial salinity under SE winds. This variation in initial salinity is possibly due to variability in estuarine mixing during previous tidal cycles and advection of saltier water off of the tidal flats into the Fraser channel due to the SE wind; the Steveston jetty would block this process under NW winds. Under NW winds, the lateral northern front of the plume was observed in the ship's radar due to the high intensity of wave breaking along the front (radar not shown, schematic in Fig. 2.1b).

Velocity profiles collected from the Robertson ADCP show different current structure under the two different wind conditions. Under SE winds, the near-surface velocity starts at 1.5 m/s in a sheared layer ∼4 m thick (Fig. 1.2c). This velocity is directed to the southwest, across the Strait, following the trajectory of the Sand Heads jetty. Soon after the drifters exit the river mouth, the surface layer velocity turns sharply to the north, as would be expected from the Coriolis effect. As it turns, the layer slows and thins to a depth of ∼1 m. This behavior is consistent with the decreasing depth of the 21 psu isohaline. By the end of the drift track, the SWIFT drift speed is 1/10th as small as its initial value. Beneath the surface layer, there is a smaller flow toward the south associated with the ebb tidal current

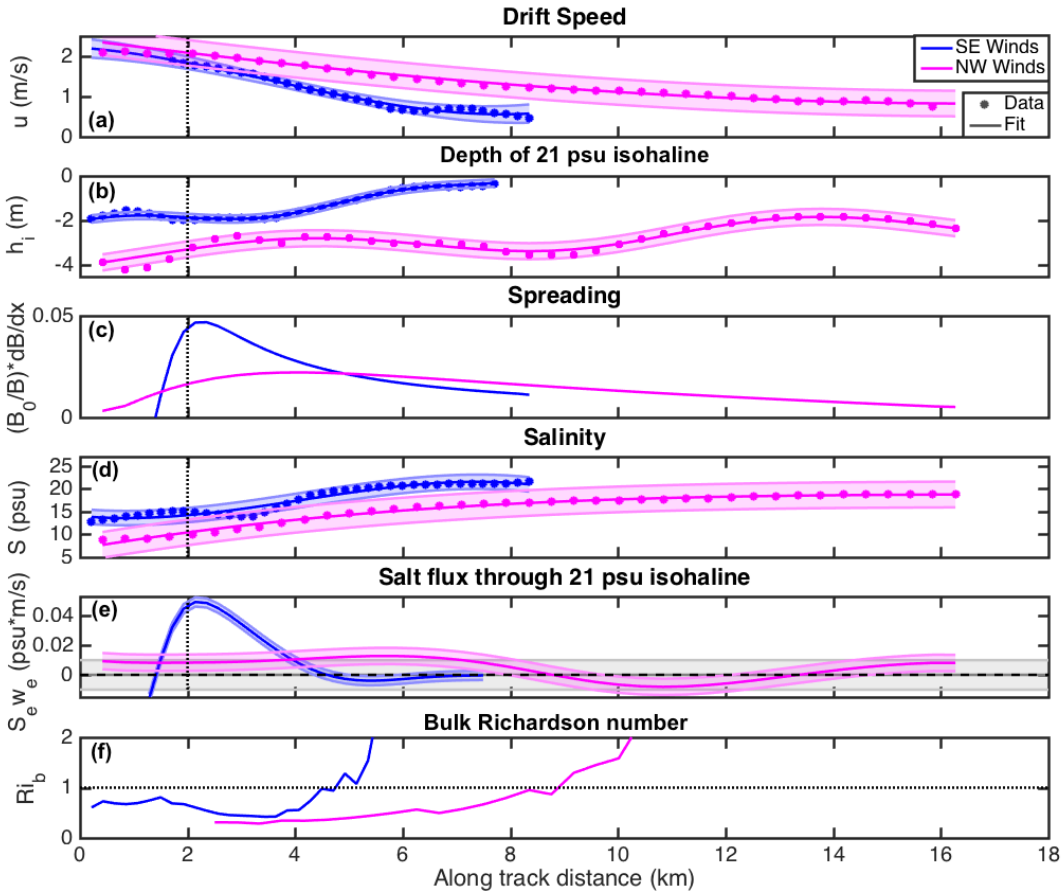

Figure 2.2: Along-track plots for SE winds (blue) and NW winds (magenta) of (a) SWIFT drift speed; (b) indicates the depth of the 21 psu isohaline, calculated from CTD casts and the SWIFT v4β CT chain; (c) indicates the non-dimensional spreading parameter, which is equal to the initial drifter separation divided by separation at an along-track distance divided by the spreading rate at that same along-track distance; (d) is the 0.5 m SWIFT salinity; (e) indicates the calculated salt flux per Eq. (1.2); (f) is the bulk Richardson number. Points indicate SWIFT data, lines indicate the cubic fit to that data, and error bars show error due to the fit.

in the Strait of Georgia. Under NW winds, the near-surface velocity starts at 2 m/s and forms a sheared layer that is ∼6 m thick (Fig. 1.2d). This velocity is directed across the Strait, controlled by the channel at Sand Heads during the beginning of the drift track, but stays directed roughly southwest throughout the entire deployment. The surface layer stays thicker for longer which is consistent with the isohaline behavior. The surface flow does not decelerate as much as under SE conditions, reaching a final velocity of 1 m/s. Tidal and wind-driven currents flow underneath the surface river outflow. Under SE winds, observed currents beneath the plume (via shipboard ADCP measurements) show currents of 50 cm/s, while a downwind measurement from an AWAC mooring shows near-surface velocities of 20 cm/s. Under NW winds, observed currents beneath the plume (via shipboard ADCP measurements) show currents of 50 cm/s, while an upwind measurement from the AWAC mooring shows near-surface currents of 60 cm/s.

Fig. 1.2 shows that the Fraser plume does not behave like a classic two-layer slab model. For both wind conditions, the water is continuously stratified and sheared in the near-field of the plume. Under SE winds, the plume evolves into a two layer system in the far-field, with a lower density layer persisting to 10 m depth, and small continuous shear to 7 m depth. Under NW winds, the plume remains continuously sheared and stratified in the far-field to a depth of ∼10 m, but the stratification and shear are of smaller magnitude than in the near-field.

2.1.3 Mixing Results

Fig. 2.2e shows along-track results for mixing calculations for two pairs of drifters under NW winds and one pair of drifters under SE winds. Under SE winds, the plume mixes vigorously ($S_e w_e = 4 \times 10^{-2} psum/s$) at the beginning of the drift track, and gradually stops mixing by $s \approx 4.5$km. Under NW winds, the plume mixes less intensely at the beginning of the drift track and continues this mild mixing until $s \approx 8.5$km. Under SE winds, the mixing appears to shut down by the point of the drift track where the plume has turned almost completely to the north.

The salt flux values obtained are roughly similar to previous studies. MC08 measured salt fluxes of 5×10^{-2} psu m/s at the Columbia, and MacDonald and Geyer [2004] measured salt flux of 1×10^{-1} psu m/s closer to the channel mouth in the Fraser; however, neither of these studies shows effects of mixing in the near field differing as a result of variable wind conditions. MC09 assumes the wind forcing does not have much influence on the plume momentum balance–this may be true for a system as energetic as the Columbia; however, the difference in the mixing behavior between the two days I have presented must be associated with the change in wind direction, as all other forcing conditions (Table 1.1) remained consistent between the two days.

Calculations of bulk Richardson number, $Ri_b = g' h_p/(\Delta u^2)$, where $g = g(\rho_0 - \rho_p)/\rho_0$, are consistent with these salt flux results (Fig. 2.2f). In these calculations, I take h_p as the depth of the 21 psu isohaline, Δu as the difference between SWIFT drift speed (to represent the plume velocity) and the velocity observed by a downlooking SWIFT just below the 21 psu isohaline (to represent the ambient velocity), ρ_p as the mean density above the 21 psu isohaline, and ρ_0 as 1021 kg/m^3 (equivalent to water of 5 $^\circ$ C and 26 psu). Taking the critical value of bulk Richardson number to be $Ri_b = 1$, I see that under NW winds $Ri_b < 1$ at the beginning of the drift track; however, Ri_b rises through the drift track and exceeds one near the halfway point, indicating a shutdown of mixing as shown in salt flux calculations. Similar behavior is observed under SE winds.

From SWIFTs with three CTs, I can see that salinity difference between 0.2 m and 1.2 m is similar for each wind condition at the beginning of the drift track (Fig. 2.3a). By the end of the drifts, however, a higher level of stratification persists under NW wind conditions than under SE wind conditions. This is consistent with my salt flux and bulk Richardson number calculations; less near-surface mixing occurs under NW wind conditions.

Average turbulent dissipation in the upper 0.7 m of the water column is higher under NW winds than under SE winds by about a factor of two 2.3b). This is likely due to the slightly higher wind velocities observed for NW wind conditions, as well as wave breaking that was apparent along the lateral northern front of the plume from the deck of the *Robertson*.

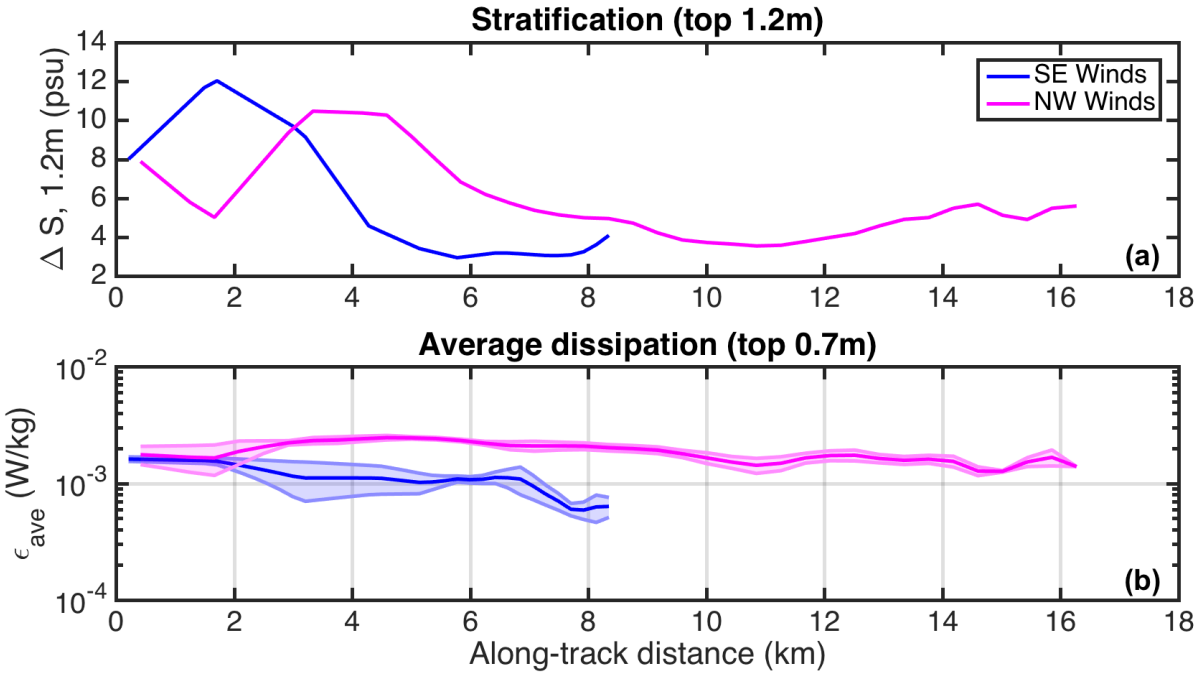

Figure 2.3: Along-track plots for SE winds (blue) and NW winds (magenta) of (a) stratification in the top 1.2 m of the water column as reported by SWIFTs with three CT sensors; (b) average TKE dissipation rate from uplooking SWIFTs in the top 0.7 m of the water column. Error bars come from variance between different SWIFTs.

This elevated turbulence with higher persistent stratification seems to be an incongruous observation. In order to understand the dynamics involved, I consider a momentum balance in the Lagrangian reference frame of the drifters.

2.1.4 Stream-Normal Momentum Balance Results

I make momentum calculations as detailed in Section 2.4 for one pair of SWIFTs for each wind condition. For NW winds, I choose the northernmost pair of SWIFTs released (the second northern-most drifters in Fig. 2.1b, which appear as one drift track due to their close proximity). For SE Winds, I choose the pair of SWIFTs released in the middle of the channel (the right-most two drifters in Fig. 2.1a). SWIFTv4β was also used to provide downlooking current profiles for the SE wind condition.

Fig. (2.4) shows stream-normal momentum balances for each wind condition. I calculate two residuals for each momentum balance: one (in burgundy) that contains the contribution from ambient current form drag and wave radiation stress gradient, if any, and one (in black) that is the result of including these contributions in the momentum balance. Under SE winds, I assume these forces do not contribute to the stream normal momentum balance. The wave radiation stress gradient in the stream normal-direction is taken as zero, as there is no significant stream-normal wave field or large stream-normal front to break such a wave field. The ambient current form drag is taken to be zero as the tidal currents in the Strait contribute to the streamwise momentum equation once the plume has turned. This is not true as the plume is turning, and so I expect a form drag contribution to the residual at the beginning of the SE wind along-track momentum balance. Thus, under SE winds, the net residual is primarily equivalent to the residual pressure gradient, as shown in Fig. 2.4a. Under NW winds, the net residual (in burgundy in Fig. 2.4b) includes both the residual pressure gradient and forcing from the wave radiation stress gradient and ambient current form drag.

Under SE winds (Fig. 2.4a), the acceleration, Coriolis, and pressure gradient residual terms dominate the stream-normal momentum balance with minor contributions from the

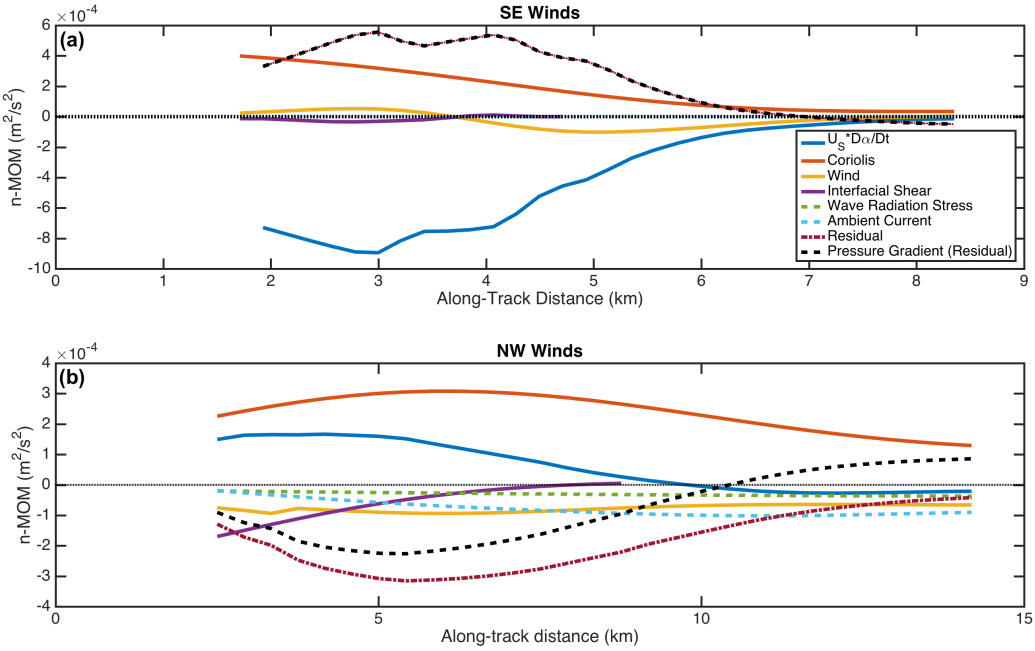

Figure 2.4: Along-track plots for depth-integrated terms in the stream-normal (n) momentum equation for (a) SE winds and (b) NW winds. Rotational acceleration is the solid blue line, Coriolis is the solid red line, wind stress is the solid gold line, interfacial shear stress is the solid purple line, wave radiation stress gradient is the dashed green line, ambient current form drag is the dashed blue line, net residual is the dash-dotted burgundy line, and pressure gradient residual is the dashed black line. The dotted black line indicates zero momentum.

wind stress and interfacial shear stress terms. The balance of Coriolis and pressure gradient forces with the acceleration indicates that the stream-normal pressure gradient and Coriolis combine to turn the plume to the right. This agrees with the numerical model results presented by MC09 and Chen et al. [2009]. The magnitude of the terms become smaller over the course of the drift track as the initial ebb tidal pulse subsides. Under NW winds (Fig. 2.4b), the stream-normal momentum balance has more important terms: in addition to acceleration, Coriolis, and pressure gradient, wind stress, interfacial shear stress contribute. The balance of Coriolis with wind stress and interfacial shear stress results in a large net residual (in burgundy on Fig. 2.4b) and a smaller stream-normal acceleration than under SE winds. The residual is smaller (in black on Fig. 2.4b) when I include approximate calculations of the wave radiation stress gradient and form drag contribution to pressure gradient, but its shape and initial sign do not change. Thus the resulting stream-normal momentum balance of Coriolis and acceleration with wind stress, interfacial shear stress, wave radiation stress gradient, ambient current form drag, and pressure gradient residual shows that the plume turns slightly to the left due to external forcing and the local pressure gradient. Reasons for this balance are examined in section 4.4. It should be noted that the wave radiation stress gradient is smaller than other terms under NW winds, with more significant terms contributing up to 2 orders of magnitude more to the momentum balance. I show in the section 4.4 that the residuals lie in line with previous work, and so this error is small relative to the signal of the pressure gradient term.

2.2 Discussion

2.2.1 Role of waves

The momentum balance approach does not indicate a clear contribution of wave dynamics; therefore, I consider an energetics approach in this section. Despite smaller waves during SE winds and larger waves breaking on the northern front of the plume during NW winds, I do not see evidence of a significant wave impact on plume mixing. In order to quantify

the effect of wave breaking on plume mixing, I compare measured near-surface turbulent dissipation rate (from SWIFTs with uplooking ADCPs) extrapolated to the depth of the 21 psu isohaline using a scaling from Terray et al. [1996] to turbulence derived from the previously calculated salt flux by assuming a mixing efficiency. I calculate the extrapolated dissipation rate, ϵ_{wave} by assuming the dissipation measured by the SWIFT is all due to wave breaking. Terray et al. [1996] define the following scaling:

$$\epsilon^{wave}(z)H_{sig} = G(\frac{z}{H_{sig}})^{-2}, \tag{2.1}$$

where G is a parameter representing the flux of turbulence through the surface that I determine by fitting $(z/H_{sig})^{-2}$ to each 10 minute average SWIFT uplooking turbulent dissipation rate profile, and represents the surface input of turbulence. Plugging in the depth of the 21 psu isohaline for z in Eq. (2.1) gives the value of wave-driven dissipation at the interface, ϵ_i^{wave}. This value is dependent on both the value of G and the depth of the isohaline, but the along-track variability of ϵ_i^{wave} closely matches that of the 21 psu isohaline depth for both wind conditions. This indicates that the isohaline depth is the dominant term in determining the value of ϵ_i^{wave}, and thus the relative importance of wind/wave mixing at the base of the plume. Fig. 2.5a shows along-track values of ϵ_i^{wave}, with values increasing from $\mathcal{O}(10^{-4})$ to $\mathcal{O}(10^{-3})$ W/kg for SE winds and remaining within $\mathcal{O}(10^{-5})$ W/kg for NW winds.

To calculate the dissipation associated with the calculated salt flux through the 21 psu isohaline, ϵ^{salt} I assume a mixing efficiency $\Gamma = 0.2$ such that

$$\epsilon^{salt} = \frac{\beta g S_e w_e}{\Gamma}, \tag{2.2}$$

where $\beta = \frac{\partial \rho}{\partial S} = 0.77 \times 10^{-3}$ is the change in density with salt. The value ϵ^{salt} is thus the total dissipation (from any turbulent source) required to generate the calculated salt flux. Fig. 2.5b shows the results from this calculation, which show peak ϵ^{salt} values of 2×10^{-3} W/kg under SE winds and peak values of 5×10^{-4} W/kg under NW winds. As the dissipation is directly proportional to the salt flux, the two quantities have identical along-track variability.

In order to compare the relative magnitudes of these two derived dissipation values, I calculate the ratio $\epsilon_i^{wave}/\epsilon^{salt}$. For the beginning of each drift track, ϵ_i^{wave} makes up 1 to 5%

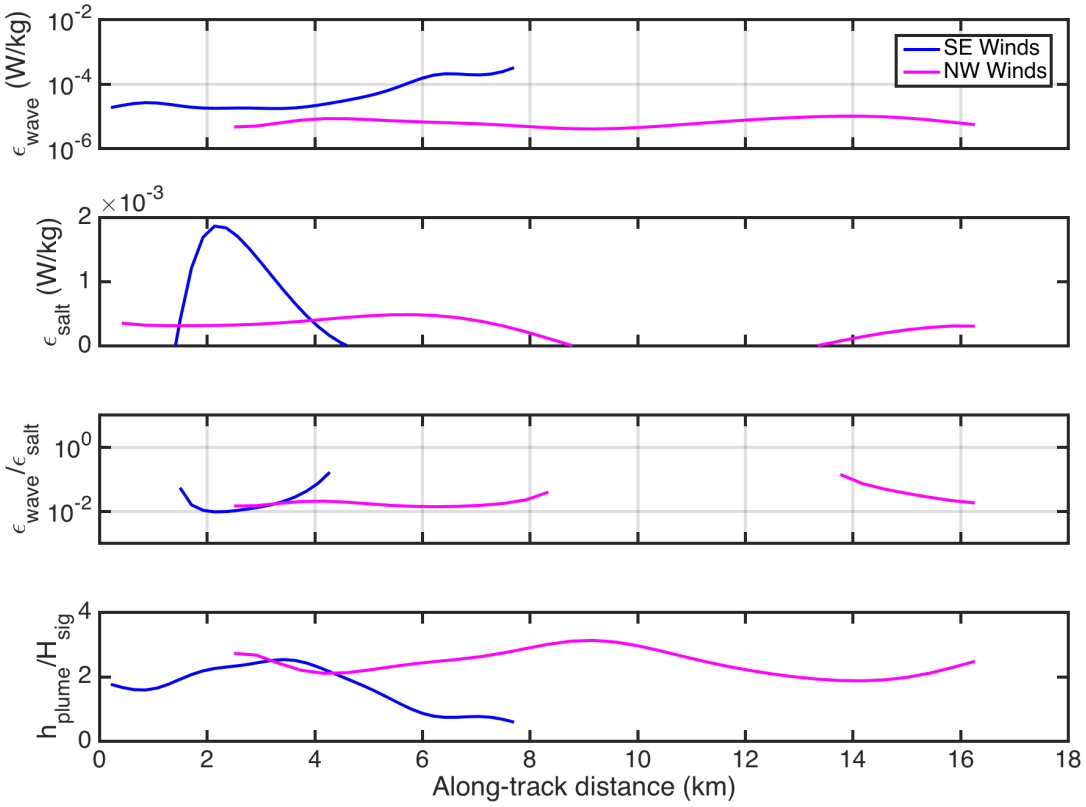

Figure 2.5: Along-track plots for (a) dissipation extrapolated from near-surface SWIFT measurements to the base of the plume in W/kg; (b) dissipation associated with salt flux through the base of the plume, in W/kg; (c) the ratio of (b) to (a); (d) The ratio of plume depth to significant wave height. All figures show results for NW winds in magenta and SE winds in blue.

of the total dissipation calculated until Ri_b becomes nearly subcritical (Fig. 2.5c). Based on the dependence of ϵ_i^{waves} with the depth of the 21 psu isohaline, it is evident that for most of the regions of higher mixing under each wind condition the plume is too deep for turbulence from wave breaking to significantly impact it. For the portions of the drift tracks where $S_e w_e > 0$, $h_p/H_{sig} \geq 2$ (Fig. 2.5d). In the open ocean, wave-driven turbulent transport balances dissipation in the turbulent kinetic energy budget to a depth of approximately $10H_{sig}$ [Terray et al., 1996, Gerbi et al., 2009]. The shallower depth presented here shows that there must be influence from the buoyancy or shear production terms in the TKE budget, which I would expect in the presence of strongly stratified surface shear layer such as a river plume. I would especially expect buoyancy and shear production to be important near the base of the plume, h_p.

Based on Thomson et al. [2014], I would expect the plume current to cause measurable wave breaking. I visually observed breaking along the lateral northern front (as well as noticing a band in the ship's radar); however, the plume current had little effect on total wave energy, as I observed nondimensional wave energy to scale with nondimensional fetch similarly to Kahma [1981] (not shown). The current had an expected effect on wave steepness: effectively opposing currents under NW winds increased spectral wave steepness, and following currents under SE winds decreased spectral wave steepness (also not shown).

2.2.2 Net Mixing

I can calculate a volumetric mixing rate by multiplying the area of the plume base by the salt flux through that portion of the plume. I calculate the area of the plume base as the trapezoid formed by a SWIFT pair over the course of two bursts, A_i, and use the associated salt fluxes to calculate net mixing (Fig. 2.6a),

$$Q_{salt} = A_i \times S_e w_e, \tag{2.3}$$

where Q_{salt} is the inflow rate of ambient saline water to the plume, indicating the net mixing rate at a point along the drift track. This calculation shows that under SE winds, when the

plume turns and spreads, the plume mixes intensely over a region ∼2 km long (1700 psu m^3/s cumulatively). This fits with the conceptual model presented by Hetland [2010], in which spreading is a primary driver of mixing. However, I observe similar Q_{salt} under NW wind conditions, when the plume is constrained by the winds. This net mixing increases slowly but persistently over the longer drift track under NW winds, reaching a similar cumulative value (1700 psu m^3/s) to the SE wind condition at the end of the SE wind region of active mixing, 4.5km. At the end of the active mixing region under NW winds (8.5 km from Sand Heads), the cumulative mixing value has increased to 9000 psu m^3/s. This indicates that the length of the active mixing region plays an important role in elevating Q_{salt} by increasing the area (Fig. 2.6b) over which the calculated salt flux acts. Thus a larger plume area can compensate for a smaller salt flux and result in a similar value of Q_{salt} for the two different wind conditions. This is similar to the findings of Yuan and Horner-Devine [2013], who have determined that the area of the base of the plume is a key factor in plume mixing. Despite this similarity, it is counter intuitive that there would be more net mixing under NW winds, when there is less spreading, as it would be expected that the loss of momentum due to shear instabilities to increase the Richardson number above critical and shut down mixing. Mixing clearly persists, indicating that either the wind and waves are a significant factor in mixing, or that the shear required to generate the smaller salt fluxes observed along track under NW winds is not large enough to increase the Richardson number above critical until 8 km into the drift track. The second explanation is more likely, as the near-surface dissipation under NW winds is of similar magnitude to that observed under SE winds, indicating that wind and wave-driven dissipation is likely to be similar for the two days.

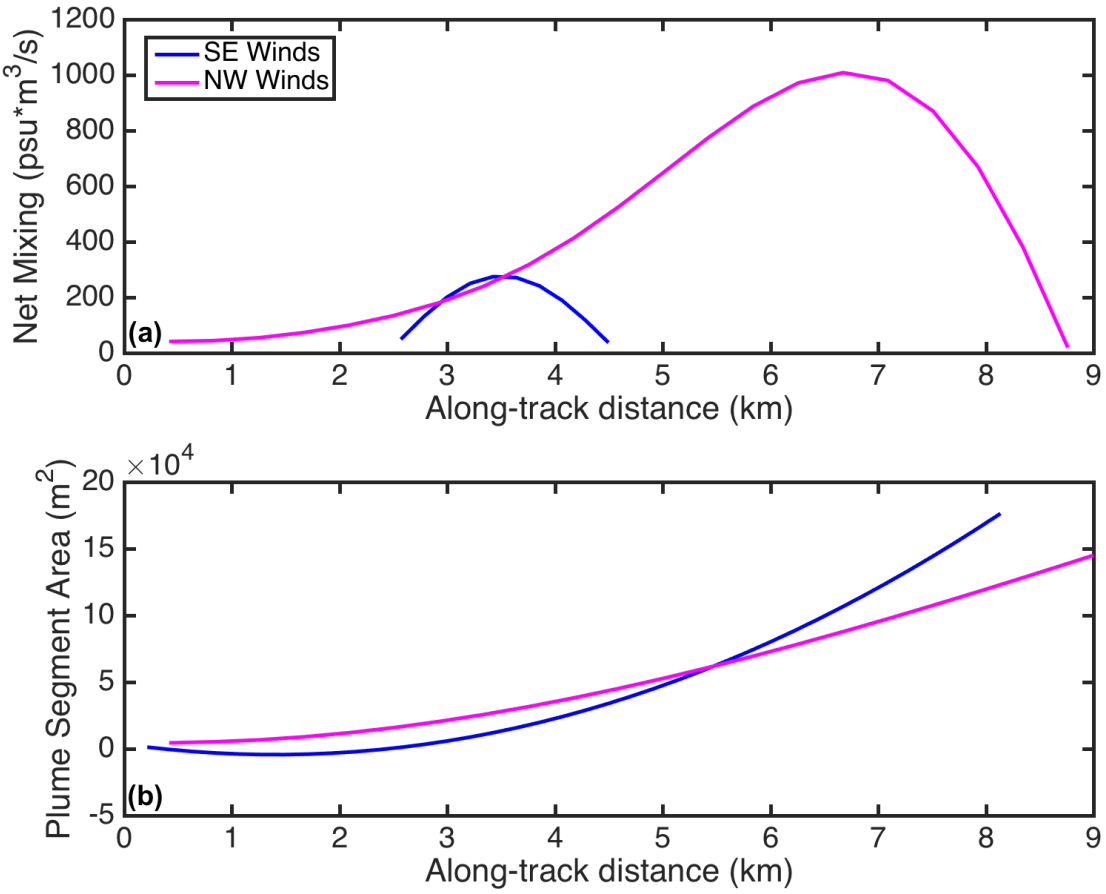

Figure 2.6: Panel (a) shows Q_{salt} along track. SE winds are represented in blue and NW winds in magenta. Panel (b) shows the area used to calculate Q_{salt} along track.

2.2.3 Comparison to spreading theory

The spreading theory developed in MacDonald and Chen [2012] and Geyer et al. [2017] shows that the interfacial drag coefficient of the plume can be parameterized by the spreading of the plume, such that

$$C_i = \alpha \frac{\Delta W}{\bar{W}} \frac{\delta}{L}, \tag{2.4}$$

where C_i is the interfacial drag coefficient,α is a constant coefficient, ΔW is a change in plume width, $\bar{W}$ is a mean plume width, δ is the depth of the mixing layer (taken to be the plume depth), and L is the streamwise length over which the plume width changes. $\phi = \frac{\Delta W}{\bar{W}} \frac{\delta}{L}$ is a spreading parameter, and Geyer et al. [2017] find $\alpha = 0.064$. Using this drag coefficient formulation, Geyer et al. [2017] calculate salt flux as

$$\overline{S'w'} = C_i \Delta S \Delta u, \tag{2.5}$$

where $\overline{S'w'}$ is a calculated salt flux, ΔS is the difference between plume salinity and ambient salinity, and Δu is the difference between plume velocity (taken to be mean drift speed for the associated pair(s) of drifters) and ambient velocity (taken to be zero). Drifter spreading measurements and $\alpha = 0.064$ yield the salt flux displayed in Fig. 2.7a. These salt fluxes are ∼20-25× smaller than those I calculate using the control volume method. I thus make a calculation of C_i such that

$$C_i = \frac{S_e w_e}{\Delta u \Delta S}, \tag{2.6}$$

where $S_e w_e$ is the salt flux calculation from Eq. 1.2. This C_i is independent of the spreading parameter ϕ, and therefore I can use the relationship in Eq. 2.4 to calculate a value of α (Fig. 2.7(a)). I find $\alpha = 1.93$ from linear regression of C_i and ϕ, which appears to be a reasonable fit from Fig. 2.7b. This value is ∼30 times higher than the value reported in Geyer et al. [2017]. As using $\alpha = 0.064$ results in salt flux values that are low relative to my calculations, it would appear that α could be sensitive to differences between plume systems.

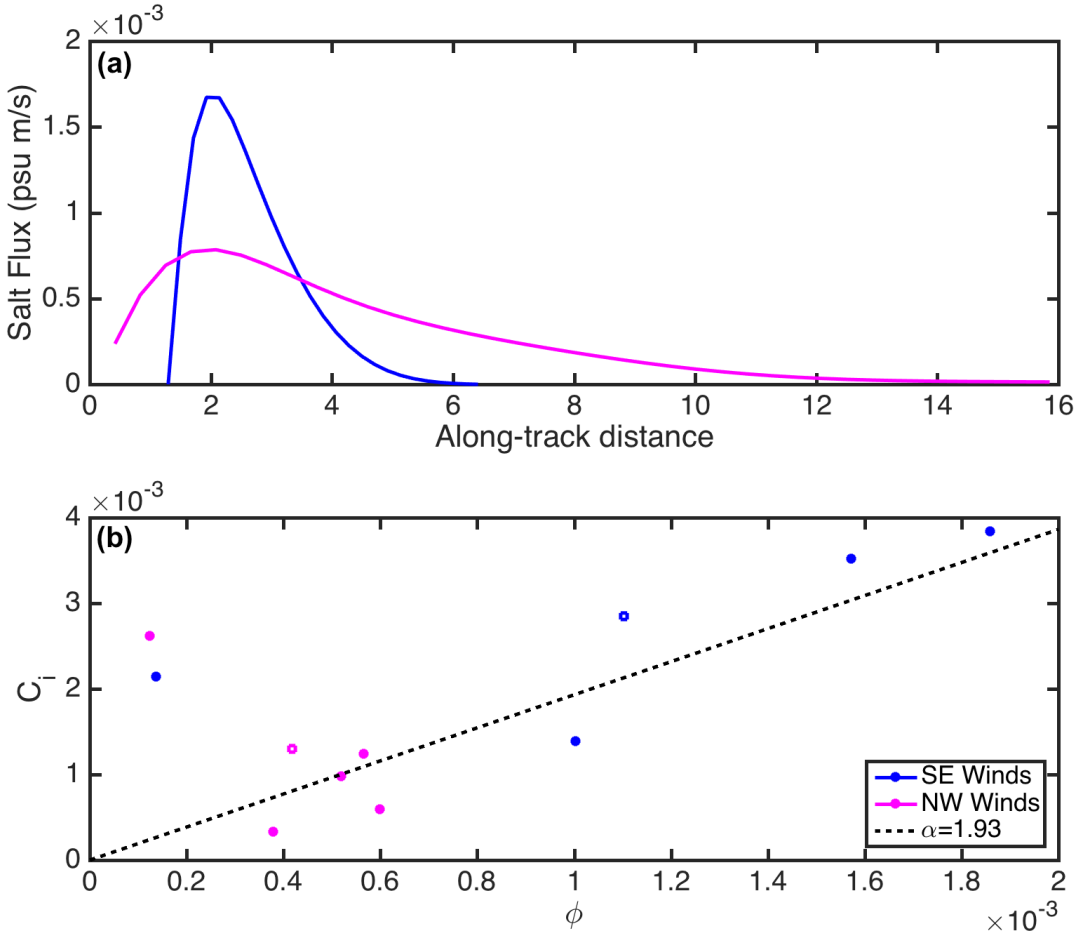

Figure 2.7: Panel (a) shows salt flux along track calculated using Eq. 2.4 and Eq. 2.5, with $\alpha = 0.064$. SE winds are in blue, and NW winds are in magenta. Panel (b) shows variability in the interfacial drag coefficient, C_i, with the spreading parameter, $\phi = \frac{\Delta W}{W}\frac{\delta}{L}$. The dashed line in black indicates $\alpha = 1.93$, which is found through linear regression. Solid points are ∼30 minute averages, and open points are deployment-long averages. SE winds are in blue, and NW winds are in magenta.

2.2.4 Spreading Effects

Mixing in a plume is classically described as a competition between spreading and shear-driven turbulence [Hetland, 2010], which is encapsulated by the Richardson number. As the plume leaves the river mouth, its high velocity relative to the ambient water drives shear instabilities, which in turn decrease this velocity. Concurrently, the plume is no longer constrained by channel geometry, and so it spreads, increasing its velocity (due to volume conservation) and its surface area available for mixing. These two processes simultaneously act to either decelerate or accelerate the plume, and in balance will hold the Richardson number at a critical value. Once one process dominates the other, the Richardson number increases and the plume stops mixing. Under SE winds, I observe $Ri_b < 1$ for half of the drift track, which is consistent with observations of salinity in the upper water column. At the beginning of the drift track (Fig. 2.2c & 2.2e), spreading drives intense mixing until the fresher river water is substantially mixed into the ambient Strait of Georgia water. Under NW winds, lower spreading values lead to smaller salt fluxes over a larger along-track distance with $Ri_b < 1$. While the net mixing under each wind condition may be the same, the physics governing these two conditions are different, as shown by stream-normal momentum balances.

Stream-normal momentum balance calculations show that wind-influenced terms and the pressure gradient stop the plume from spreading under NW winds (Fig. 2.4b). The effect of wind stress, interfacial shear stress, and ambient current form drag is relatively straightforward to understand, as these are all external forces that push or drag on the plume. The ambient current and its associated interfacial shear stress are important to the stream-normal momentum balance under NW winds only because it is in this configuration that they are aligned with the ebb tidal current in the Strait. The combination of these two currents creates a strong near-surface flow in the Strait that collides with and subducts under the plume due to the higher density of ambient Strait water. This imparts a form drag on the plume (partially compensated by a baroclinic pressure gradient at the front associated

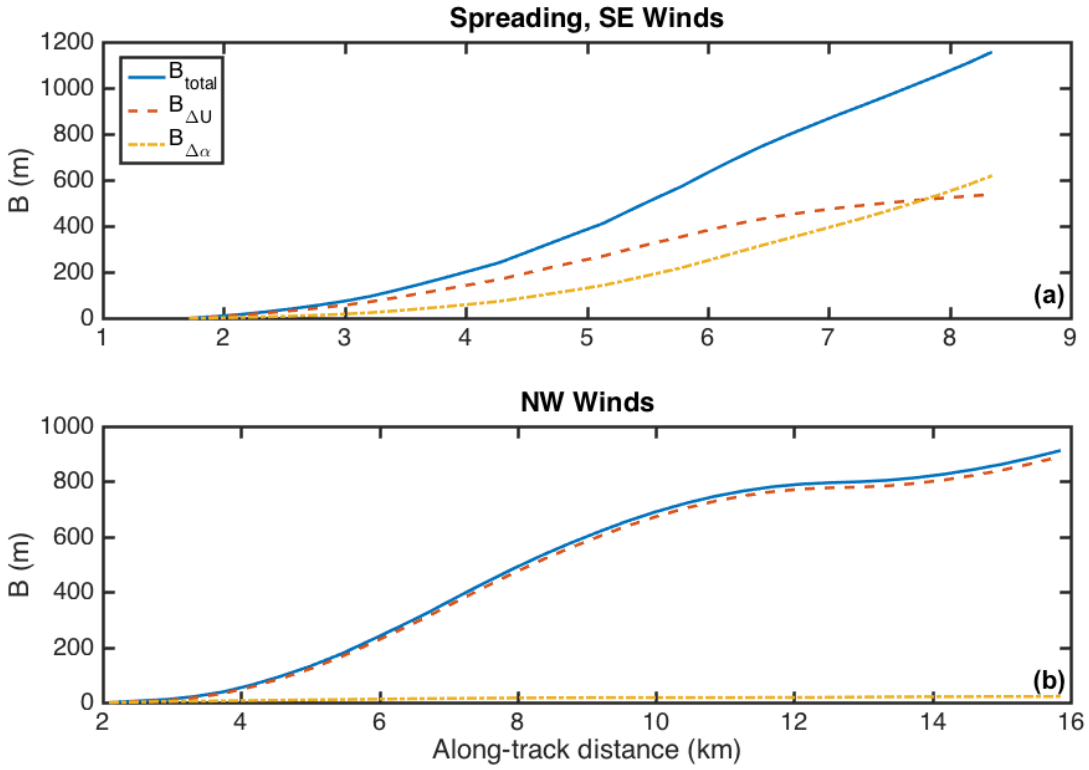

Figure 2.8: Along-track plots for spreading component terms under (a) SE winds and (b) NW winds from the same drifter pairs as the momentum calculations. Solid blue lines represent spreading, which is calculated from Eq. (2.7), dashed red lines represent spreading due to differences in drift speed, and dash-dotted gold lines represent spreading due to difference in drift angle.

with frontal tilt, O'Donnell et al. [1998]) and causes interfacial shear stress as it subducts. Under SE winds, the wind stress and its associated current are in opposition to the ebb tidal velocity, which should result in slower near-surface flow; I lack observations south of the plume to corroborate this hypothesis. Additionally, the ebb tidal flow out of the NW would be incorporated in the streamwise momentum balance once the plume turns under SE wind influence, and thus would not increase the stream-normal interfacial shear stress after this point.

To better understand the calculated pressure gradient residual, I turn to methods from

MC09, where numerical simulations show that a dome of freshwater associated with max ebb is important in setting up initial flow conditions. Even with the symmetric stream-normal pressure gradient resulting from a freshwater dome, Coriolis still leads to asymmetric plume spreading, as it opposes the pressure gradient on the left half of the plume and aligns with it on the right half (left/right in the streamwise reference frame). This leads to more rightward spreading than leftward spreading in the northern hemisphere. MC09 notes that drifter spreading can be caused by along-track differences in drift speed or drift angle between a drifter pair, and that the dominant of these spreading terms can differentiate which part of the freshwater dome the drifters transect. MC09 calculates these spreading terms by defining a rate of spreading as a difference between the velocity vectors associated with two drifters as follows:

$$d\vec{U} = \vec{U}_b - \vec{U}_a = \frac{D\vec{B}}{Dt} = \sqrt{U_b^2 + U_a^2 - 2U_bU_a\cos(\alpha_b - \alpha_a)}. \tag{2.7}$$

Spreading, B, can be found by integrating Eq. (2.7), where U_a, U_b represent drift speeds of two drifters, and α_a, α_b represent drift directions of the same two drifters. MC09 finds the portion of spreading associated with only the drift speeds by finding and integrating in time $\frac{DB_{\Delta U}}{Dt} = dU = U_2 - U_1$, which does not include drift angle. Spreading associated with angular differences, $B_{\Delta\alpha}$ is then calculated as a residual, such that $B_{\Delta\alpha} = B - B_{\Delta U}$. Thus, $B_{\Delta\alpha}$ may be thought of as spreading influenced by the stream-normal momentum balance, and $B_{\Delta U}$ may be thought of as spreading influenced by variability of the streamwise momentum balance between streamlines.

There is a difference between the south (left) and north (right) sides of the plume: spreading is dominated by $B_{\Delta U}$ on the south side and is more evenly distributed between the terms on the north side. This is consistent with the balance between stream-normal pressure gradient and Coriolis discussed above. Performing this spreading analysis on the drifter releases, I see that under SE winds (Fig. 2.8a), the drifters experience spreading due to a combination of drift speed and angle differences. This is similar to expectations for the north side of the plume, which experience a positive stream-normal pressure gradient, the same sign as the residual momentum balance term for SE winds. Under NW winds (Fig. 2.8b), I see that

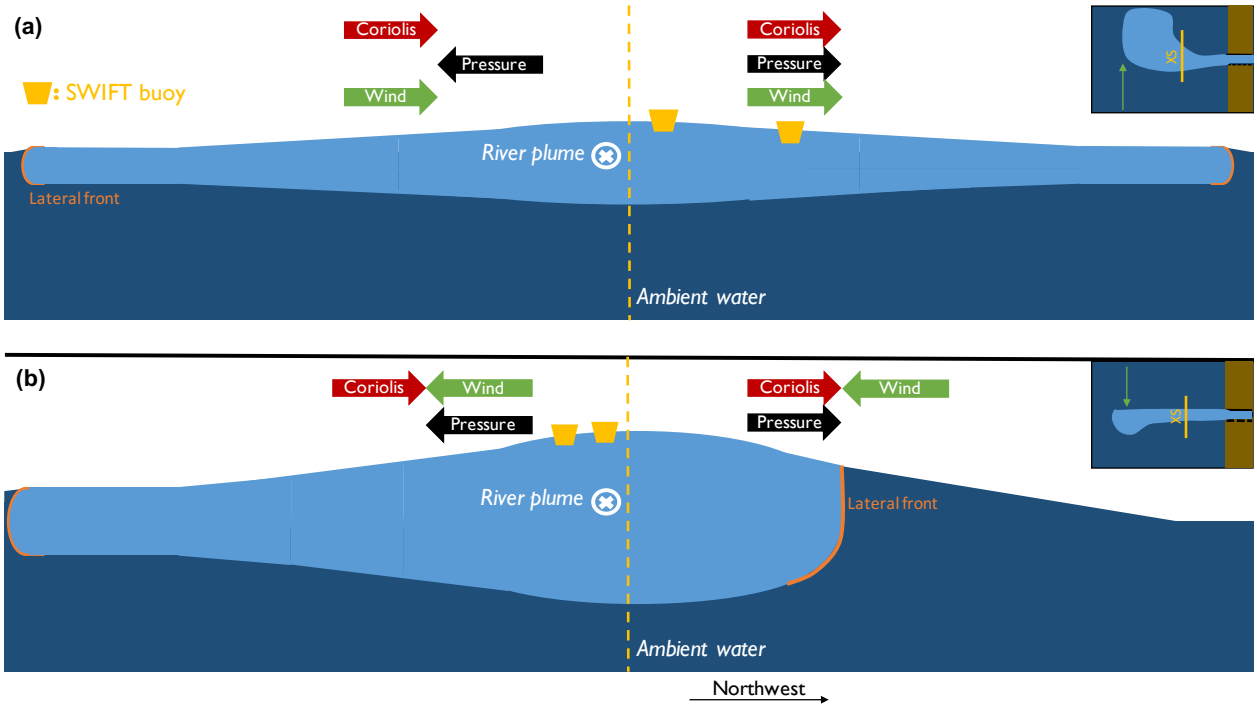

Figure 2.9: Schematic of plume reconfiguration. Panel (a) shows downwelling (SE) winds and panel (b) shows upwelling (NW) winds. For each wind condition, I show a stream-normal cross section of the plume looking down-current relative to the plume velocity offshore of the river mouth. Arrows indicate direction of momentum terms for each sector of the plume, trapezoids indicate SWIFT drifters and insets show plan view.

the drifters experience spreading mostly due to drift speed differences, which is consistent with the small rotational accelerations that I calculate in the momentum balance. This is most similar to expectations for drifters released on the south side of the plume, which experience a negative stream-normal pressure gradient, and is the same sign as the residual for NW winds. This drifter pair was released the furthest to the right in the channel mouth of the three deployments that day and stayed close to the northern front, indicating that the stream-normal pressure gradient and Coriolis are in opposition near the right-most edge of the plume under NW winds. The sign of the pressure gradient is confirmed under both wind conditions by the GPS elevation data from the SWIFTs (not shown). This is a departure from the interpretation by MC09 that the stream-normal pressure gradient and Coriolis are aligned on the right (streamwise) side of the plume. In order to reconcile this difference, I hypothesize that under NW wind forcing the plume forms a "half-dome" like feature over most of which stream-normal pressure gradient and Coriolis are in opposition (Fig. 2.9). Since the only forcing condition that has changed between the two days is the wind speed and direction, this implies that the wind can change the shape of the sea surface height anomaly associated with the freshwater plume, causing a change in the interaction of the stream-normal pressure gradient and Coriolis force that leads to less spreading and mixing as the plume becomes pinched between these opposing forces.

2.3 Summary

I have shown that under two different wind conditions, I observe different behavior, mixing, and dynamics in the near-field Fraser River plume on an ebbing tide. Under SE winds, the plume thins, spreads, turns to the right, and mixes intensely due to a stream-normal momentum balance dominated by rotational acceleration, pressure gradient, and Coriolis. Under NW winds, the plume stays thicker and narrower while propagating directly across the Strait of Georgia, mixing less intensely. This is due to a combination of wind stress, an ambient current in the Strait, interfacial shear stress, and pressure gradient opposing Coriolis. These opposing forces pinch the plume, preventing it from mixing. I observe wave

contributions to mixing and momentum over the whole surface layer to be small, although small but significant near-surface turbulence is observed under NW wind conditions. The longer zone of active mixing under NW winds results in a larger cumulative volumetric salt flux into the plume despite lower salt fluxes per unit area, indicating that the area of the region of active mixing plays a key role in the net mixing of the plume. Calculations of the causes of plume spreading show that under NW wind conditions, the wind can reconfigure the sea surface height anomaly associated with the plume, although direct estimates of this behavior will be necessary in future work.

BIBLIOGRAPHY

C. Akan, S. Moghimi, Ozkan-Haller H. T., Osborne J., and Kurapov A. On the dynamics of the mouth of columbia river: Results from a three-dimensional fully coupled wave-current interaction model. *J. Geophys. Res.*, 122(7):n/a–n/a, 2017.

M. L. Banner, A. V. Babanin, and I.R. Young. Breaking probability for dominant waves on the sea surface. *J. Phys. Oceanogr.*, 30:3145–3160, 2000.

A. Chawla and J. T. Kirby. Monochromatic and random wave breaking at blocking points. *J. Geophys. Res.*, 107(C7):4–1–4–19, 2002. ISSN 2156-2202.

F. Chen, D. G. MacDonald, and R. D. Hetland. Lateral spreading of a near-field river plume: observations and numerical simulations. *J. Geophys. Res.*, 114:C07013, doi:10.1029/2008JC004893, 2009.

P.D. Craig and M.L. Banner. Modeling wave-enhanced turbulence in the ocean surface layer. *J. Phys. Oceanogr.*, 24(12):2546–2559, 1994.

F. Dobson, W. Perrie, and B. Toulany. On the deep-water fetch laws for wind-generated surface gravity waves. *Atmos.-Ocean*, 27:210–236, 1989.

M.A. Donelan, J. Hamilton, and W. H. Hui. Directional spectra of wind-generated waves. *Phil. Trans R. Soc. Lond. A*, 315(1534):509–562, 1985.

F. Feddersen. Observations of the surfzone turbulent dissipation rate. *J. Phys. Oceanogr.*, 42:386–399, 2012a.

F. Feddersen. Scaling surf zone turbulence. *Geophys. Res. Lett.*, 39(18 (L18613)), 2012b.

D. A. Fong and W. R. Geyer. Response of a river plume during an upwelling favorable wind event. *J. Geophys. Res.*, 106(C1):1067–1084, 2001.

I. García Berdeal, B. M. Hickey, and M. Kawase. Influence of wind stress and ambient flow on a high discharge river plume. *J. Geophys. Res.*, 107(C9):doi:10.1029/2001JC000932, 2002.

J. Gemmrich. Strong turbulence in the wave crest region. *J. Phys. Oceanogr.*, 40:583–595, 2010.

G. Gerbi, S. E. Kastner, and G. Brett. The role of whitecapping in thickening the ocean surface boundary layer. *J. Phys. Oceanogr.*, 45(8):2006–2024, 2015.

Gregory P Gerbi, John H Trowbridge, Eugene A Terray, Albert J Plueddemann, and Tobias Kukulka. Observations of turbulence in the ocean surface boundary layer: Energetics and transport. *J. Phys. Oceanogr.*, 39(5):1077–1096, 2009.

Gregory P. Gerbi, Robert J. Chant, and John L. Wilkin. Breaking surface wave effects on river plume dynamics during upwelling-favorable winds. *J. Phys. Oceanogr.*, 2013/08/05 2013.

W. R. Geyer, J. H. Trowbridge, and M. M. Bowen. The dynamics of a partially mixed estuary. *J. of Phys. Oceanogr.*, 30:2035–2048, 2000.

W. R. Geyer, D. K. Ralston, and R. C. Holleman. Hydraulics and mixing in a laterally divergent channel of highly stratified estuary. *J. Geophys. Res.*, 122(6):4743–4760, 2017.

J. L. Hench and R. A. Leuttich. Transient tidal circulation and momentum balances at a shallow inlet. *J. Phys. Oceanogr.*, 33(4):913–932, 2003.

R. D. Hetland. Relating river plume structure to vertical mixing. *J. Phys. Oceanogr.*, 35(9): 1667–1688, 2005.

R. D. Hetland. The effects of mixing and spreading on density in near-field river plumes. *Dyn. Atmos. Oceans*, 49:37–53 doi:10.1016/j.dynatmoce.2008.11.003, 2010.

B. M. Hickey, L. J. Pietrafesa, D. A. Jay, and W. C. Boicourt. The Columbia River Plume Study: Subtidal variability in the velocity and salinity fields. *J. Geophys. Res.*, 103(C5): 10,339–10,368, 1998.

B. M. Hickey, S. Geier, N. Kachel, and A. MacFayden. Ebb-tide dynamics and spreading of a large river plume. *Continental Shelf Research*, 25(14):1631–1656, 2005.

G. Hoekstra. Proposed route would bring kinder morgan pipeline closer to fraser river. *Vancouver Sun*, 101(172):n/a–n/a, 2013.

A. R. Horner-Devine, David Jay, P. Orton, and E. Spahn. A conceptual model of the strongly tidal Columbia River plume. *J. Mar. Sys.*, 78:460–475, 2009.

A.R. Horner-Devine, R. D. Hetland, and D.G. MacDonald. Transport and mixing in coastal river plumes. *Ann. Rev. of Fluid Mech.*, 47:569—594, 2015.

E. J. Hunter, R. J Chant, J. L. Wilkin, and J. Kohut. High-frequency forcing and subtidal response of the Hudson River plume. *J. of Geophys. Res.*, 115:doi:10.1029/2009JC005620, 2010.

J. T. Jurisa, J. D. Nash, J. M. Moum, and L.F. Kilcher. Controls on turbulent mixing in a strongly stratified and sheared tidal river plume. *J. Phys. Oceanogr.*, 46(8):2373–2388, 2016.

K. K. Kahma. A study of the growth of the wave spectrum with fetch. *J. Phys. Oceanogr.*, 11(11):1503–1515, 1981.

G. Kakoulaki, D.G. MacDonald, and A.R. Horner-Devine. The role of wind in the near field and midfield of a river plume. *Geophys. Res. Lett.*, 2014.

L. Kilcher, J.D. Nash, and J. N. Moum. The role of turbulence stress divergence in decelerating a river plume. *J. Geophys. Res.*, 117(C05032), 2012.

S. Lentz. The Response of Buoyant Coastal Plumes to Upwelling-Favorable Winds. *J. Phys. Oceanogr.*, 34(11):2458–2467, 2004.

S. J. Lentz and J. Largier. The influence of wind forcing on the chesapeake bay buoyant coastal current. *J. Phys. Oceanogr.*, 36(7):1305–1316, 2006.

D. G. MacDonald and F. Chen. Enhancement of turbulence through lateral spreading in a stratified-shear flow: Development and assessment of a conceptual model. *J. Geophys. Res.*, 117(C05025):doi:10.1029/2011JC007484, 2012.

D. G. MacDonald and W. R. Geyer. Turbulent energy production and entrainment at a highly stratified estuarine front. *J. Geophys. Res.*, 109:C05004, doi:10.1029/2003JC002094, 2004.

D. G. MacDonald, L. Goodman, and R. D. Hetland. Turbulent dissipation in a near-field river plume: A comparison of control volume and microstructure observations with a numerical model. *J. Geophys. Res.*, 112:C07026, doi:10.1029/2006JC004075, 2007.

R. McCabe, B. M. Hickey, and P. MacCready. Observational estimates of entrainment and vertical salt flux in the interior of a spreading river plume. *J. Geophys. Res.*, 113(C08027), 2008.

R McCabe, P MacCready, and B. M. Hickey. Ebb-tide dynamics and spreading of a large river plume. *Journal of Physical Oceanography*, 39(11):2839–2856, 2009.

C.C. Mei. *The Applied Dynamics of Ocean Surface Waves*, volume 1 of *Advanced Series on Ocean Engineering*. World Scientific, 1989.

W. K. Melville. The role of surface-wave breaking in air-sea interaction. *Annu. Rev. Fluid Mech.*, 28:279–321, 1996.

James O'Donnell, George O. Marmorino, and Clifford L. Trump. Convergence and Downwelling at a River Plume Front. *J. Geophys. Res.*, 28:1481–1495, 1998.

M. Guerra Paris and J. Thomson. Turbulence measurements from 5-beam acoustic doppler current profilers. *J. Atmos. Ocean. Tech.*, in minor revision (http://faculty.washington.edu/jmt3rd/Publications/FiveBeamGuerraThomsonRevised.pdf), 2017. doi: http://faculty.washington.edu/jmt3rd/Publications/FiveBeamGuerraThomsonRevised.pdf.

Z. Rong, R. D. Hetland, W. Zheng, and X. Zhang. Current-wave interaction in the mississippi-atchafalaya river plume on the texas-louisiana shelf. *Ocean Modelling*, 84(1): 67–83, 2014.

J. Sharples, J. J. Middleburg, K. Fennel, and T. D. Jickells. What proportion of riverine nutrients reaches the coastal ocean? *Global Biogeochem. Cycles*, 31(1):39–58, 2017.

E. A. Terray, M. A. Donelan, Y. C. Agrawal, WM Drennan, K. K. Kahma, A. J. Williams, P. A. Hwang, and S. A. Kitaigorodskii. Estimates of kinetic energy dissipation under breaking waves. *J. Phys. Oceanogr.*, 26(5):792–807, 1996.

J. Thomson. Wave breaking dissipation observed with SWIFT drifters. *J. of Atmos. and Ocean. Tech.*, 29(12):1866–1882, 2013/01/03 2012.

J. Thomson, E. A. D'Asaro, M. Cronin, E. Rogers, R. Harcourt, and A. Schcerbina. Waves and the equilibrium range at Ocean Weather Station P. *J. Geophys. Res.*, 2013.

J. Thomson, A. R. Horner-Devine, S. Zippel, C. Rusch, and W. Geyer. Wave breaking turbulence at the offshore front of the columbia river plume. *Geophys. Res. Letters*, 41:8987–8993, 2014. ISSN 1944-8007. doi: 10.1002/2014GL062274. URL `http://dx.doi.org/10.1002/2014GL062274`.

J. Thomson, M. S. Schwendeman, S. F. Zippel, S. Moghimi, J. Gemmrich, and W. E. Rogers. Wave-breaking turbulence in the ocean surface layer. *J.*

Phys. Oceanogr., 46(6):1857–1870, 2016. doi: 10.1175/JPO-D-15-0130.1. URL http://dx.doi.org/10.1175/JPO-D-15-0130.1.

I.R. Young. *Wind Generated Ocean Waves*. Elsevier Ocean Engineering Book Series. Elsevier, New York, 1999.

Y. Yuan and A.R. Horner-Devine. Laboratory investigation of the impact of lateral spreading on buoyancy flux in a river plume. *J. Phys. Oceanogr.*, 43(12):2588–2610, 2013.

X. Zhang, M. Marta-Almeida, and RD Hetland. A high-resolution pre-operational forecast model of circulation on the Texas-Louisiana continental shelf and slope. *J. of Op. Oceanogr.*, 5(1):19–34, 2012.

S.F. Zippel and J. Thomson. Wave breaking and turbulence at a tidal inlet. *J. Geophys. Res.*, 120(2):10161031, 2015.

Appendix A

PLUME EFFECTS ON WAVES

In order to quantify the effect of the Fraser River plume on the incident wave field in the Strait of Georgia, I turn to analysis based on fetch and wave steepness. The plume current would be expected to induce wave-breaking on the northern front present under NW winds [Thomson et al., 2014], which would be apparent in fetch analysis as a deficit of wave energy relative to expectations (based on empirical fetch laws) for a given fetch. Currents are known to affect wave steepness, as waves steepen on an opposing current and flatten on a following current.

A.1 Fetch Analysis

In the open ocean, wave energy typically scales with the duration and distance over which the wind blows [Young, 1999]. At first, the duration of the wind dictates wave energy, and after a time $t < 77.23\frac{X^{0.67}}{U^{0.34}g^{0.33}}$ (where X is the distance over water the wind blows, the fetch, and U is the wind velocity), the fetch dictates the wave energy. This relationship can be described empirically by a power law such that $\hat{H} = A\hat{X}^b$ and $\hat{T}_p = C\hat{X}^d$, where A, b, C, and d are empirical constants. $\hat{H}$ is a nondimensional wave height such that $\hat{H} = \frac{gH}{U_{10}^2}$ (where H is wave height and U_{10} is wind speed), $\hat{T}_p$ is a nondimensional peak wave period such that $\hat{T}_p = \frac{gT_p}{U_{10}}$ (where T_p is the peak wave period) [Young, 1999], and $\hat{X} = \frac{gX}{U_{10}^2}$. The constants A, b, C, and d have been shown to vary between studies [Kahma, 1981, Donelan et al., 1985, Dobson et al., 1989, Young, 1999]. The Strait of Georgia is similar to the Bothnian Sea in that it is a semi-enclosed basin, and thus a reasonable comparison for fetch analysis would be the relationship developed by Kahma [1981].

For the fetch calculations presented here, I use SWIFT buoy data to compare $\hat{X}$ and $\hat{H}$.

SWIFT significant wave height is taken to be H_{sig}, and the SWIFT wind speed measurement is extrapolated to U_{10} assuming a log-layer wind speed profile. I take the fetch, X, to be equal to the distance from the buoy to land in the measured wind direction. I found little variation in results when I used various combinations of SWIFT wind data, wind data from the Sand Heads weather station, the bathymetry of the Strait, and an elliptical geometrical approximation of the Strait. I can thus calculate a non-dimensional wave energy and fetch for every SWIFT burst, where the nondimensional wave energy is $\hat{E} = \frac{g^2 H^2}{16 U_{10}^4}$ (Fig. A.1).

Counter to expectations, there does not appear to be a significant difference in the relationship between fetch and wave energy under the varying wind conditions present during the study period (Fig. A.1). There is significant scatter in the data, but generally it appears that nondimensional energy scales with nondimensional fetch, represented reasonably well by the relationship from Kahma [1981]. There is not a noticeable difference in the relationship under SE and NW wind conditions.

This result suggests that wave breaking at a plume front (as presented in Thomson et al. [2014]) does not result in a large loss of wave energy. I note that the data presented in Thomson et al. [2014] from the Columbia plume feature currents that directly oppose a wave field, whereas the NW wind conditions from the study feature a front parallel to the plume current. Here, the wave-field propagates on the following ambient current until it reaches the plume, at which point this current is no longer present. This has the same effect as an opposing current of the same magnitude, generating the wave breaking observed at the front. This "opposing current" is not as strong as the opposing current measured at the leading plume front (propagating across the Strait under NW winds) or at the front of the Columbia plume [Thomson et al., 2014], where energetic wave breaking has been observed.

A.2 Steepness Analysis

Wave steepness is a major controlling parameter of wave breaking, as waves tend to break when $Hk > 1/7$, where H is wave height and k is wavenumber [Mei, 1989]. As previously explained, wave frequency can be modified by Doppler shift due to opposing or following

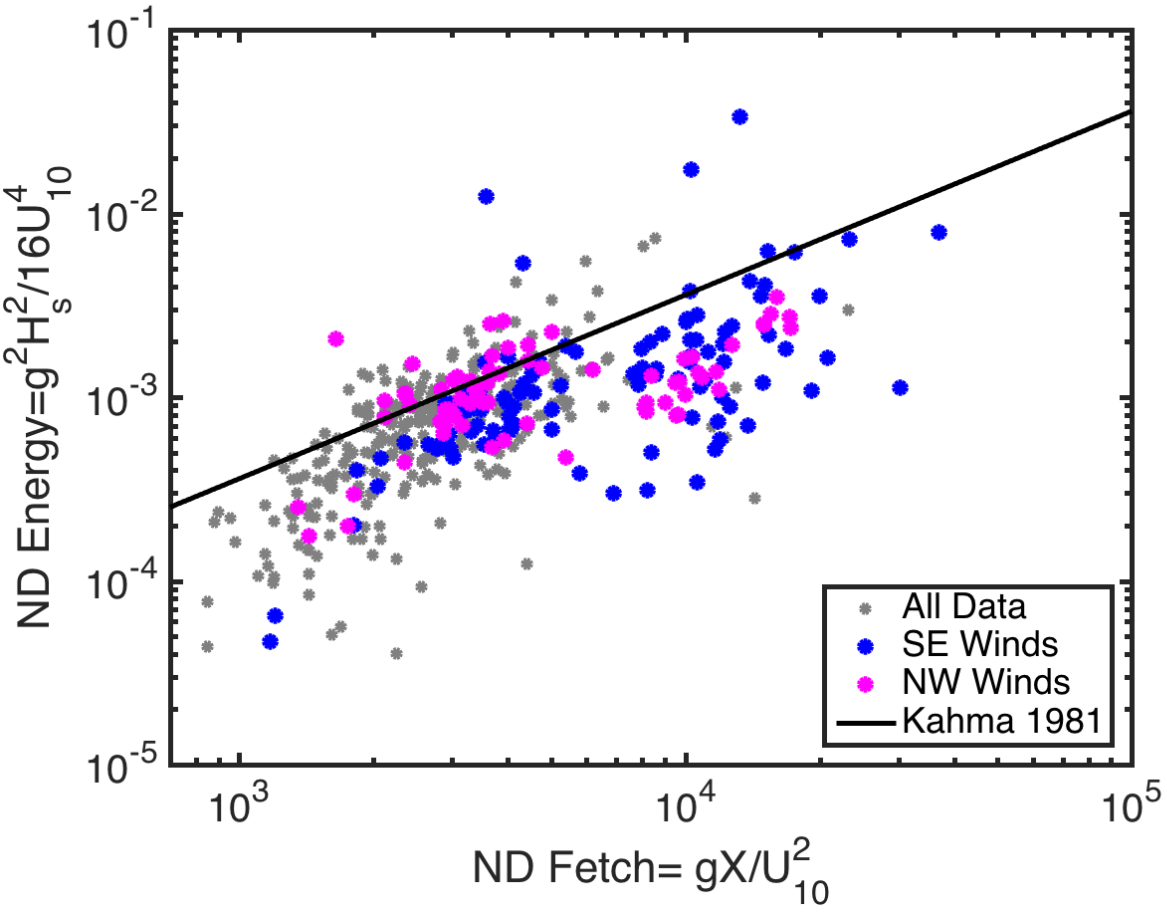

Figure A.1: Scatter plot showing the relationship of $U_d \cos(\theta_{wave} - \theta_d)$, the component of drift speed in the direction of wave propagation, with $MSS_{intrinsic} - MSS_{absolute}$, the difference in absolute vs intrinsic mean square slope. Brown points are from the Columbia plume with an energetic wind sea, green points are from the Columbia plume with minimal wind sea, blue points are from the Fraser plume under SE winds, and magenta points are from the Fraser plume under NW winds. Each data point represents half an hour of SWIFT buoy data.

currents (Eq. 1.1). This modification leads to a change in wave steepness, which is similar to the spectral mean square slope,

$$MSS = \int \frac{(2\pi f)^4 E(f)}{g^2} df \tag{A.1}$$

where f is a wave frequency and $E(f)$ is the spectral energy at this frequency [Thomson et al., 2013]. Thus I can calculate a mean square slope for both the absolute frequency and the intrinsic frequency by taking $f = \omega$ or $f = \sigma$, respectively, such that

$$MSS_{absolute} \propto E\omega^4 \tag{A.2}$$

$$MSS_{intrinsic} \propto E\sigma^4. \tag{A.3}$$

The quantity $MSS_{intrinsic}$ is the spectral mean square slope associated with the intrinsic frequency, E is the wave energy, $MSS_{absolute}$ is the spectral mean square slope associated with the absolute frequency, σ is the intrinsic frequency, and ω is the absolute frequency. The difference $MSS_{intrinsic} - MSS_{absolute}$ shows the effect of the current-induced Doppler shift on the spectral mean square slope, which is proportional to the slope squared, H^2k^2. A positive value of $MSS_{intrinsic} - MSS_{absolute}$ indicates waves that have steepened. This difference would scale with the relative direction of the wave-field and currents.

In order to calculate the effect of the plume on wave steepness, I calculate the difference between the spectral mean square slope using the absolute wave frequency and the intrinsic wave frequency using SWIFT observations of wave spectra, drift speed, and drift direction. I compare this to the component of drift speed in the direction of the wave field, $U_d \cos(\theta_{wave} - \theta_d)$, where U_d is the drift speed, θ_{wave} is the direction of the wave field, and θ_d is the drift direction. In Fig. A.2, I present average values over half an hour of deployment time.

Results show that waves are steepened under opposing currents and flattened under following currents (Fig. A.2). Of the four data sets presented in Fig. A.2, the Columbia plume with a large opposing wind sea shows a large increase in steepness, and the strongest opposing currents. The Fraser plume under NW winds shows a similar increase in steepness but a weaker opposing current, and some waves on following currents (likely in the interior

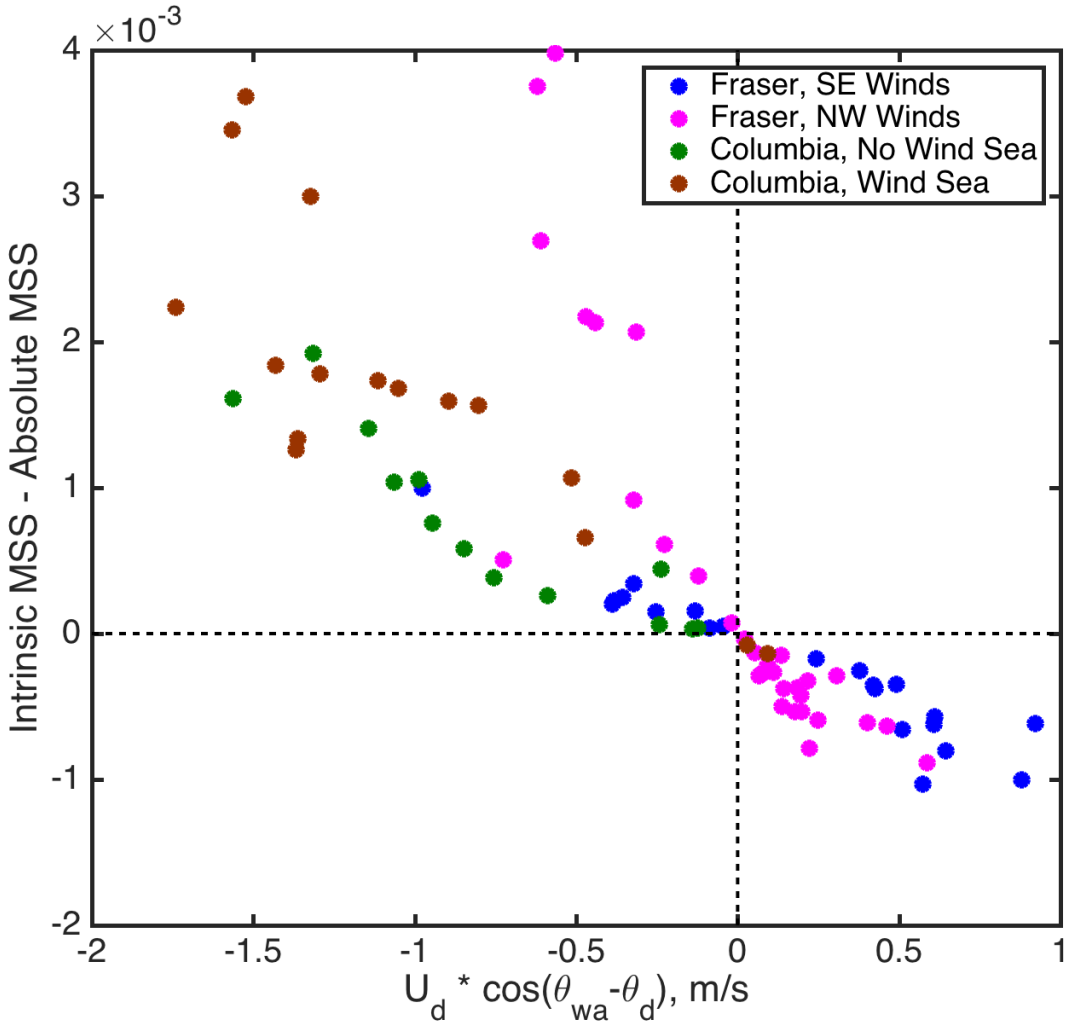

Figure A.2: Scatter plot showing the relationship of $U_d \cos(\theta_{wave} - \theta_d)$, the component of drift speed in the direction of wave propagation, with $MSS_{intrinsic} - MSS_{absolute}$, the difference in absolute vs intrinsic mean square slope. Brown points are from the Columbia plume with an energetic wind sea, green points are from the Columbia plume with minimal wind sea, blue points are from the Fraser plume under SE winds, and magenta points are from the Fraser plume under NW winds. Each data point represents half an hour of SWIFT buoy data.

of the plume). The Columbia plume with a small opposing wind sea shows a smaller increase in steepness, but a stronger opposing current than the Fraser. Under SE winds conditions in the Fraser plume, the wave steepness is lowered under following currents.

There is autocorrelation present in Fig. A.2 such that $MSS_{intrinsic} - MSS_{absolute}$ is linearly related to $-U_d \cos(\theta_{wave} - \theta_d)$, so the clear linear relationship is likely spurious. However, the data sets I present sort along the x and y axes, indicating that different conditions can span this parameter space. The lower maximum steepness difference at the Columbia with a small opposing wind sea compared to a larger opposing wind sea is likely due to preferential breaking of wind waves at the front with a more energetic wind sea [Thomson et al., 2014]. This fits with the change in steepness observed under NW winds at the Fraser, as the wave field in the Strait is predominantly a wind sea. Thus although the plume current under NW winds does not remove a significant amount of energy from the ambient wave field in the Strait of Georgia, the current does impact wave steepness. This steepness effect falls in line with data from the Columbia River plume, and fits with results presented in Thomson et al. [2014], where wind waves preferentially break at the Columbia River plume front.